sustainability

MDPI

Article

A Data-Driven Latent Digital Twin Framework for Sustainable Agroecosystem Management

Aigul Mimenbayeva [1], Tamara Zhukabayeva [2], Shafiullah Khan [3,*], Gulzhan Muratova [4] and Valentina Makhatova [5]

[1] School of Artificial Intelligence and Data Science, Astana IT University, Astana 010000, Kazakhstan; a.mimenbayeva@astanait.edu.kz
[2] School of AI+X, Qazaq AI Research University, Astana 010000, Kazakhstan; tamara.zhukabayeva@qairu.edu.kz
[3] College of Systems and Computer Engineering, Abdullah Al Salem University, Khaldiya 72303, Kuwait
[4] Department of Computer Science, Kazakh Agrotechnical Research University Named After S. Seifullin, Astana 010000, Kazakhstan; g.muratova@kazatu.edu.kz
[5] Department of Software Engineering, Kh. Dosmukhamedov Atyrau University, Atyrau 060011, Kazakhstan; mahve@mail.ru
* Correspondence: shafiullah.khan@aasu.edu.kw

Abstract

In recent years, digital twins have been increasingly used in agroecosystem management. However, integrating heterogeneous satellite observations into a unified framework remains challenging. This study developed a latent-state Digital Twin framework using Sentinel-2, MODIS, and SMAP observations from 23 agricultural fields at the North Kazakhstan Agricultural Experimental Station (NKAES) LLP during 2020–2025. These observations were combined with NASA POWER meteorological data. A three-dimensional multilayer perceptron autoencoder (MLP-AE-3D) was used to represent vegetation, thermal, and soil moisture conditions in a unified latent space. The model achieved a test R^2 of 0.9654. To model temporal dynamics, MLP, GRU, and TSN architectures with different hidden dimensions were evaluated. GRU-512 was selected as the temporal prediction model, achieving a test R^2 of 0.7962 and an RMSE of 0.0749. A Kalman-based Latent Assimilation Unit (LAU) was used to update predicted latent states while accounting for uncertainty. The adaptive J-RA-LAU configuration further reduced the RMSE to 0.0701. Controlled climate-stress scenarios were used to assess latent-state and vegetation responses to heat, drought, and compound environmental stressors. The proposed framework provides a unified dynamic representation to support field-level monitoring, climate-stress assessment, and sustainable agroecosystem management.

Keywords: remote sensing; machine learning; digital twin; multisource data fusion; autoencoder; Kalman Filter; agroecosystems; latent state

Check for updates

Academic Editor: Hone-Jay Chu

Received: 2 August 2026
Revised: 19 October 2026
Accepted: 21 October 2026
Published: 29 October 2026

Copyright: © 2026 by the authors. Licensee MDPI, Basel, Switzerland. This article is an open access article distributed under the terms and conditions of the Creative Commons Attribution (CC BY) license.

1. Introduction

In recent years, agriculture has been facing challenges such as water scarcity, adverse weather conditions, and low soil fertility. The adoption of digital technologies in agriculture enables the effective management of crop fields [1–3]. In particular, remote sensing data obtained from satellites such as Sentinel-1, Sentinel-2, and Landsat help assess the condition of vegetation cover [4–6]. The types of satellite data vary according to the sensors used. Fusing data from different satellite sources, such as optical and radar data, enables a more in-depth analysis of agricultural fields. Optical satellite data commonly include red (RED)

and near-infrared (NIR) spectral bands, which are used to calculate vegetation indices based on differences in light absorption and reflection.

Geospatial data processing tools support the analysis of satellite observations [7]. Satellite observations are also used to estimate precipitation [8] and predict crop yields [9].

Vegetation indices are widely used for crop recognition, vegetation monitoring, and the assessment of crop conditions and vegetation dynamics [10–12]. Multitemporal satellite observations from Sentinel and Landsat missions have also been used for crop classification using machine learning approaches [13]. Machine learning and artificial neural network approaches have also been applied to agricultural yield forecasting in Kazakhstan [14,15].

In addition, thermal and microwave data can be used to estimate the land surface temperature (LST) and soil moisture (SM), respectively [16–18].

These variables are important for assessing the thermal and moisture conditions of crops. Synthetic Aperture Radar (SAR) data are largely independent of cloud cover and illumination conditions. They enable monitoring of soil moisture, vegetation structure, and the physical properties of the land surface [18–20]. However, individual data sources may provide limited information when analyzed in isolation. Therefore, recent studies have focused on improving monitoring accuracy by combining optical and radar data to leverage their complementary characteristics [20,21].

Oroud et al. [22] demonstrated that the combined use of NDVI and LST helps identify crop stress conditions more accurately. Recent studies have explored soil moisture modeling using Sentinel-1/2 and agroclimatic data [23]. Other studies have investigated land surface temperature downscaling to improve spatial detail [24].

Dorigo et al. [17,25] investigated the characteristics and evaluation of ESA CCI Soil Moisture products.

Previous studies have used both linear and nonlinear methods to analyze multisource remote sensing data. Autoencoders provide another approach for learning latent representations from heterogeneous observations. However, dimensionality reduction alone does not provide a dynamic representation of the agroecosystem state [26]. A remaining challenge is to integrate multisource observations into a common latent state that can evolve over time and support scenario-based analysis. Nonlinear visualization methods such as t-SNE, while capable of uncovering hidden clusters, are not designed for dynamic system modeling [27].

In this regard, autoencoders and variational autoencoders play a significant role in processing satellite data. Autoencoders have been used to learn compact latent representations and identify underlying data patterns [28,29]. Wang et al. [30] explored feature-guided masked autoencoders for representation learning in remote sensing.

Zhu et al. [31] noted in their review that deep learning methods have achieved some success in classifying and segmenting land surface features. Adrian et al. [32] demonstrated that combining optical and radar data using deep learning models can improve crop type mapping accuracy.

Berger et al. [33] reviewed the potential of multi-sensor optical data for crop stress detection and monitoring.

Despite these advances, remote sensing studies of agricultural lands generally do not model the continuously evolving latent dynamic state of the ecosystem. They mostly involve classification, segmentation, and forecasting.

Recent studies have explored ways to reconstruct ecosystem dynamics and capture changes in environmental conditions over time [34,35].

In this regard, the latent state of croplands can be considered part of a dynamic Digital Twin representation [36,37], which is updated over space and time. That is, integrating multispectral data into nonlinear models enables the construction of the latent state of

agroecosystems. Such a Digital Twin representation should possess dynamic, updatable, and scenario-analysis capabilities.

Digital Twin approaches in agriculture can employ different modeling strategies. These include biophysical, data-driven, hybrid, and dynamic state-space approaches. Biophysical approaches use process-based models to represent crop and environmental processes. Data-driven approaches use observations and machine learning methods [38,39]. Hybrid approaches combine process-based and data-driven methods. Physics-informed neural networks (PINNs) integrate physical knowledge into learning-based models [40]. Dynamic state-space models represent changes in the system state over time. They also allow new observations, including remote sensing data, to be assimilated into the model [41].

The distinction between digital twins and traditional digital systems in the literature is related to the level of integration between the digital representation and the physical system. For example, Kritzinger et al. [42] distinguish among digital models, digital shadows, and digital twins. A digital model does not involve automated data exchange. A digital shadow supports automated data flow from the physical system to its digital representation, while a digital twin enables automated bidirectional data exchange. In agriculture, integrating data from different sources remains a challenge for digital twin development [43,44].

Several functions have been identified in the literature as key characteristics of the digital twin concept. These include physical and digital entities, observations, dynamic state representation, analytical services, and state synchronization [45,46]. Based on these concepts, this study incorporates six functional properties of a digital twin. Specifically, these include a physical counterpart, observation and sensing, digital-state representation, dynamic-state evolution, state synchronization, and analytical services. The architecture of the proposed digital twin framework is presented in Section 2.4.

Tagarakis et al. [47] state that building robust digital twins of agricultural ecosystems requires a comprehensive effort. They mention the need for multisource data, appropriate processing methods, and the continuous updating of the system.

In their review, Wang et al. [48] noted a growing interest in using digital twins in agriculture. However, many studies remain at the experimental level without fully developed digital twin systems.

Some recent studies, in particular Khan et al. [49], integrated different data sources and digital twin concepts for ecological modeling. Their study demonstrated that a data-driven digital twin can integrate multiple data sources and modeling components.

While digital twins have been explored for industrial process monitoring [50], their application to climate-driven agroecosystem digital twins using multisource remote sensing data remains largely unexplored.

Overall, remote sensing-driven digital modeling represents a promising direction for monitoring agroecosystem dynamics under climate variability, enabling management-oriented insights at the field scale. However, existing remote sensing and GeoAI approaches often focus on classification or yield prediction [51]. A unified representation of agroecosystem state dynamics remains a challenge.

Recent advances in multisource data fusion and deep learning have improved the integration of optical, thermal, and soil moisture observations. These methods often lack a formal dynamic state interpretation and are not explicitly designed to support scenario-based analysis within a digital twin framework. Furthermore, challenges related to multisource data harmonization, temporal consistency, and system-level representation create a methodological gap between remote sensing analytics and the development of operational digital twins for agricultural systems.

To address this gap, the present study proposes a remote sensing-based digital twin framework. In this framework, the agroecosystem state is represented within a dynamic

latent feature space derived from multisource satellite observations. The proposed approach aims to provide a data-driven representation of agroecosystem dynamics. This representation supports temporal analysis and climate-related scenario exploration at the field scale.

Objective of the Study

The objective of this study is to develop a data-driven Digital Twin framework for representing agroecosystem states using multisource remote sensing data. The framework includes six functional properties: a physical counterpart, observation and sensing, digital-state representation, dynamic-state evolution, state synchronization, and analytical services. These properties distinguish the framework from a standalone time-series model.

Accordingly, this study addresses the following research questions:

RQ1. Can multisource Earth observation data be represented in a common latent space while preserving the main agroecosystem information?

RQ2. Can the temporal evolution of the latent agroecosystem state be modeled under changing climate conditions?

RQ3. Can observation-driven assimilation improve the synchronization of predicted and observed latent states?

RQ4. How does the learned agroecosystem state respond to controlled climate-stress scenarios?

The main contributions of this research are as follows:

- A data-driven Digital Twin framework for an agroecosystem based on multisource remote sensing data was proposed.
- A nonlinear latent-state representation was implemented and evaluated to capture the agroecosystem state from multisource Earth observation data.
- A single nonlinear model was used to integrate vegetation, thermal, and soil moisture information within a common latent space.
- A Kalman-based assimilation method was implemented to update the predicted latent state using available observations while accounting for uncertainty.
- The temporal evolution of the latent agroecosystem state was modeled and evaluated using a climate-conditioned GRU.
- Controlled climate-stress scenarios were used to evaluate the response of the learned latent states to changes in climatic conditions.

The proposed Digital Twin framework is designed as a modular analytical component that can be integrated into operational remote sensing monitoring systems.

2. Materials and Methods

2.1. Study Area

The study area is the NKAES LLP, located in the North Kazakhstan region of the Republic of Kazakhstan. The study area lies between 69°00′ and 69°45′ E longitude and 54°50′ and 55°25′ N latitude. The experimental station is located in the forest-steppe zone of Northern Kazakhstan.

The geographical location of the study area and the distribution of agricultural fields at NKAES LLP are shown in Figure 1.

The climate of the study area is sharply continental. Winters here are long and cold, and summers are relatively warm. During the growing season (May–September), average temperatures range from 14 °C to 20 °C, and the annual air temperature ranges from +1 °C to +3 °C. Annual precipitation averages 300–350 mm. Most of the precipitation falls during the summer months, particularly in June and August. Due to the uneven

distribution of precipitation during the growing season, drought is prevalent in the North Kazakhstan region. Therefore, crops grown in this region are strongly affected by soil moisture availability and heat stress.

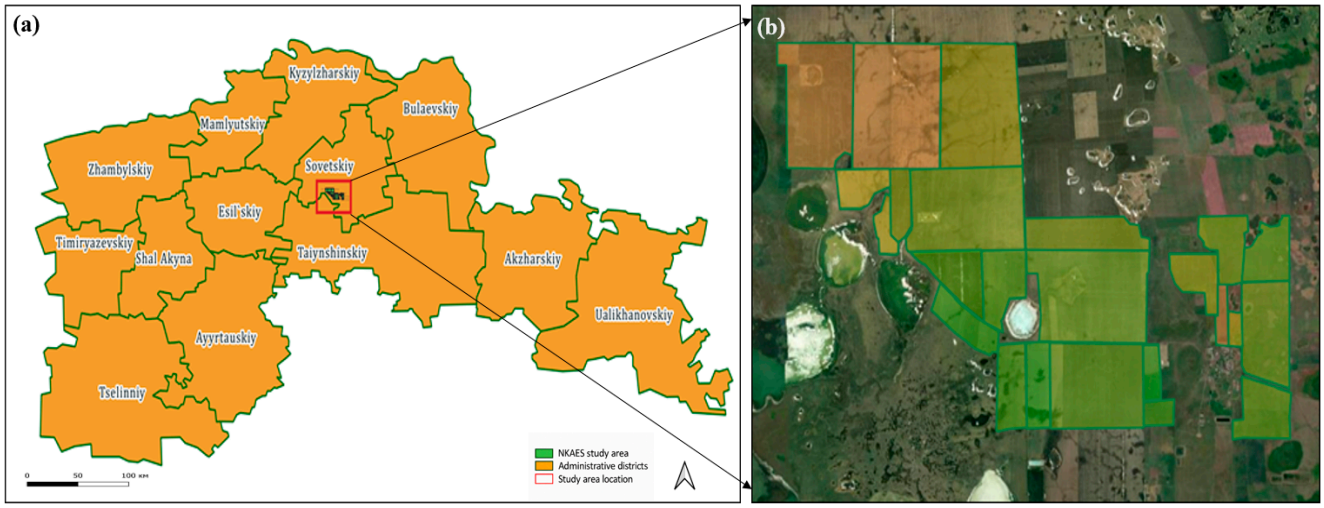


Figure 1. Location of the study area: (**a**) administrative districts of North Kazakhstan Region, Kazakhstan, with the NKAES site highlighted in red; (**b**) satellite view of agricultural fields at NKAES.

In agriculture, this region primarily grows spring wheat. Additionally, barley and oilseed crops are cultivated in experimental fields.

2.2. Remote Sensing Data Sources

In this study, data were obtained from various satellite sources to characterize vegetation cover conditions, soil moisture, and land surface thermal properties. In addition to optical data, microwave data were also used to obtain additional information.

2.2.1. Optical Data

Sentinel-2 remote sensing data were used to characterize crop conditions. These satellite data are available at spatial resolutions of 10 m, 20 m, and 60 m. Sentinel-2 provides observations in 13 spectral bands, covering the near-infrared (NIR) and shortwave infrared (SWIR) regions. Sentinel-2 remote sensing data were accessed through the Google Earth Engine (GEE) platform. The 2020–2025 growing seasons were selected as the study period. Vegetation indices such as NDVI, NDRE, and MSAVI, which characterize the conditions of vegetation, were calculated using filtered pixel values.

2.2.2. Soil Moisture Data

Information on soil moisture for the fields of the NKAES LLP was obtained from the SMAP (Soil Moisture Active Passive) Level-4 satellite product. It allows for the estimation of surface soil moisture by combining satellite observations with model estimates. The SMAP data have a daily temporal resolution and an approximate spatial resolution of 9 km. Using these data, it is possible to analyze soil moisture variations associated with crop water stress in the North Kazakhstan region.

2.2.3. Surface Temperature Data

The land surface temperature of the study fields was obtained from the NASA Terra satellite using the MOD11A2 product. The MOD11A2 product provides 8-day composite land surface temperature data at a 1 km spatial resolution. The satellite-derived values were converted to temperature values using a standard scaling factor.

Surface temperature is an important indicator of the energy balance of the agroecosystem and heat stress affecting plants. Therefore, an increase in temperature can directly affect the physiological state of plants and their productivity.

The remote sensing dataset covered the growing seasons from May 2020 to September 2025. Data were collected from May to September of each year across 23 agricultural fields. The initial pixel-level dataset contained 18,259,050 records. After selecting complete temporal series, 608,635 pixels had observations for all 30 monthly time steps.

2.3. Use of Generative AI

ChatGPT (GPT-6, OpenAI) was used solely to assist in creating illustrative icons for schematic figures. The scientific content, data, and interpretation of the figures were determined by the authors.

2.4. Data Preprocessing and Feature Engineering

2.4.1. Data Fusion and Harmonization

The remote sensing datasets used in the study were processed in the Google Earth Engine (GEE) environment. Sentinel-2, MODIS, and SMAP Level-4 data were aligned within a common spatiotemporal framework. Along with the main vegetation indices used in the study, their anomaly (deviation) values were also calculated.

In agricultural settings, satellite indices exhibit a specific seasonal cycle. For example, NDVI (Normalized Difference Vegetation Index) typically increases in spring and decreases in autumn. When the original index values are used directly, their seasonal cycle may dominate the learned representation. The anomaly values represent deviations from typical seasonal conditions. Therefore, the anomaly-based variables enable better characterization of deviations associated with drought, heat stress, abnormal vegetation development, and excess moisture.

Table 1 describes the variables obtained from Sentinel-2, MODIS, and SMAP Level-4 data.

The Sentinel-2 spectral bands listed in Table 1 were used to derive the vegetation indices and were not directly included as latent-state inputs. Correlation analysis is described in Section 3.1. Based on the results, NDVI, NDRE, NDWI, LST, and SM were selected as inputs for the latent states. This selection reduced redundancy while preserving complementary information on vegetation, water, and thermal characteristics.

Because the data sources have different spatial resolutions, a harmonization step was performed before integration. Sentinel-2 observations were quality filtered using SCL and cloud-shadow masks. The resulting dataset was spatially aligned to a common analysis grid. A window length of 5 and a second-order polynomial were used for Savitzky–Golay smoothing. To select these parameters, window lengths of 3, 5, 7, and 9 and polynomial orders 1, 2, and 3 were compared. The selected configuration provided a reasonable balance between smoothing and the preservation of temporal variability. The smoothed anomaly data had an average correlation of 0.919 with the unsmoothed values. Signal variability was reduced by 20.31%.

During the growing season, temporal synchronization was performed at monthly intervals. For Sentinel-2, monthly median composites were calculated, while MODIS LST and SMAP soil moisture were aggregated to monthly mean values. The resulting dataset was used for anomaly calculation, temporal smoothing, and latent-state construction. The preprocessing workflow is illustrated in Figure 2.

Table 1. Source remote sensing measurements and derived agroecological variables used in this study.

	Satellite, Resolution	Type/Variable	Feature	Description
Optical	Sentinel-2, 10–20 m	Spectral bands	B2, B3, B4, B5, B6, B7, B8, B8A, B11, B12	Surface reflectance in the visible, NIR, and SWIR regions
		Vegetation indices	NDVI, EVI, MSAVI, NDRE, ReCI, NDWI	Indicators of canopy greenness, chlorophyll content, and vegetation water status
		Vegetation index anomalies	NDVI_anom, EVI_anom, MSAVI_anom, NDRE_anom, ReCI_anom, NDWI_anom	Deviations from typical seasonal conditions
Hydrological	SMAP Level-4, 9 km	Soil moisture	SM_surface	Estimated moisture content in the soil surface
		Soil moisture anomalies	SM_surface_anom	Soil moisture deficit or surplus relative to the climatological norm
Thermal	MODIS, 1 km	Thermal variable	LST	Land surface temperature related to the surface energy balance
		Thermal anomaly	LST_anom	Land surface temperature deviation from typical seasonal conditions

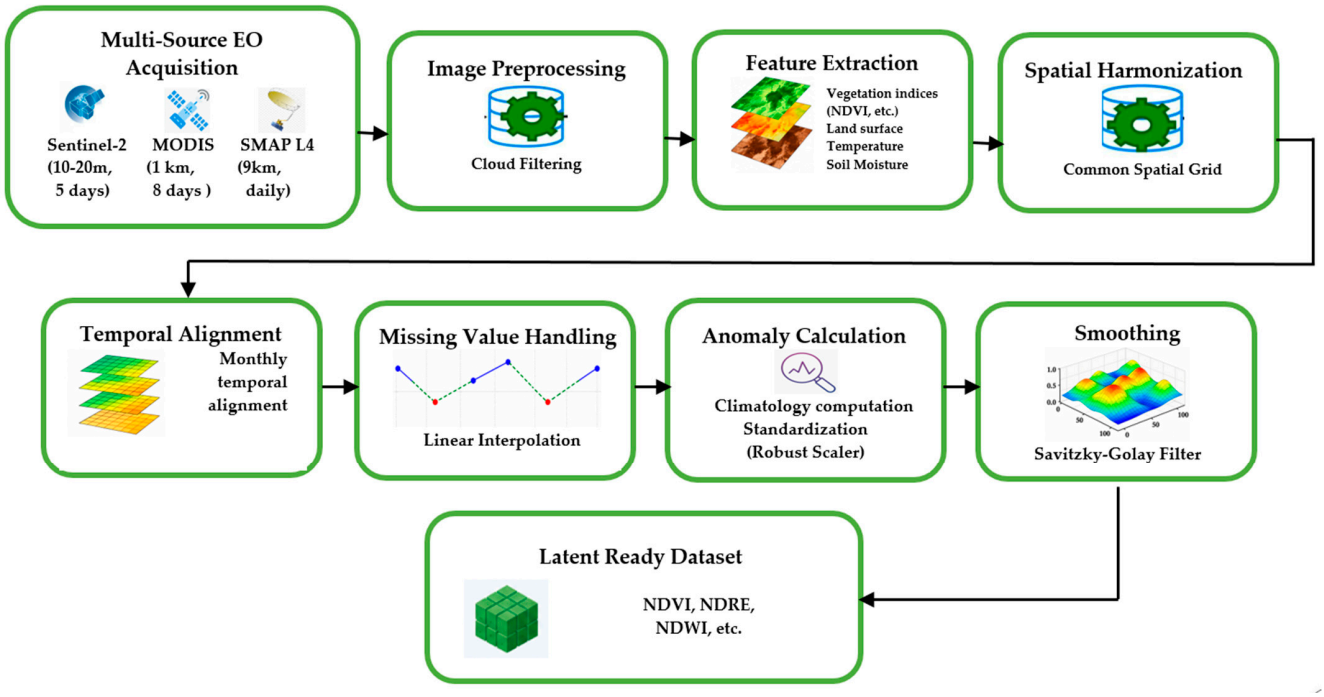


Figure 2. Preprocessing workflow for constructing the latent-ready agroecological dataset.

Harmonization steps aim to strike a balance between noise reduction and preserving short-term variability. Monthly aggregation reduces residual noise but may dampen short-term fluctuations. The spatial resampling of MODIS and SMAP was used solely for computational alignment and does not restore information beyond their native spatial resolutions. Therefore, the preprocessing strategy prioritizes robust monthly-to-seasonal agroecosystem dynamics over short-term or subpixel variability.

2.4.2. Spatial-Resolution Sensitivity Analysis

To assess the sensitivity of the coarse-resolution inputs, an additional controlled experiment was conducted. The resampled MODIS LST and SMAP soil moisture values were replaced with field–year–month means, while the Sentinel-2-based NDVI, NDRE, and NDWI remained unchanged. The anomaly calculation and Savitzky–Golay smoothing were performed again. The same RobustScaler and frozen MLP-AE-3D model were used without retraining. Sensitivity was assessed using MAE, RMSE, normalized RMSE (NRMSE), and Pearson's correlation coefficient (r).

To account for differences in variable scale, the RMSE was normalized by the standard deviation of the original data as follows:

$$NRMSE = \frac{RMSE}{\sigma_{original}} \times 100, \quad (1)$$

where $\sigma_{original}$ denotes the standard deviation of the original data, lower NRMSE values indicate smaller differences relative to the variability of the original data.

2.4.3. Time Series Post-Processing

Missing values in the time series were filled using linear interpolation. Interpolation was performed separately for each field as follows, assuming a linear change between adjacent observations:

$$X_{comp}^{int}(t) = x_{comp}(t_1) + \frac{t - t_1}{t_2 - t_1}[x_{comp}(t_2) - x_{comp}(t_1)], \quad (2)$$

where:

$X_{comp}^{int}(t)$—interpolated index at time t,

$x_{comp}(t_1)$ and $[x_{comp}(t_2)]$–the nearest available observations,

t_1, t_2—corresponding observation times ($t_1 < t < t_2$).

In the next step, the monthly deviations were calculated by subtracting the average monthly index value from the index value obtained from each observation as follows:

$$X_i^{anom}(t) = X_i^{int}(t) - \overline{X}_{i,m}, \quad (3)$$

where:

X_i^{anom}(t)—anomaly value of variable i at time t;

$X_i^{int}(t)$—interpolated value of variable i at time t;

$\overline{X}_{i,m}$—mean value of variable i for month m across the study period (2020–2025).

These derived monthly anomaly values were smoothed to reduce short-term fluctuations and random noise using a Savitzky–Golay filter as follows:

$$X_i^{anom,s}(t) = \sum_{j=-k}^{k} c_j X_i^{anom}(t + j), \quad k = \frac{w - 1}{2}, \quad (4)$$

where c_j denotes the Savitzky–Golay convolution coefficients, w is the window length, and p is the polynomial order.

2.4.4. Feature Preparation and Latent Representation

For each agricultural field f at time t, let us consider the following multivariate vector:

$$X_{f,t}^{anom,s} = \left[V_{f,t}^{anom,s}, SM_{f,t}^{anom,s}, LST_{f,t}^{anom,s}\right] \quad (5)$$

Here, $V_{f,t}^{anom,s}$ denotes the smoothed anomalies of the vegetation indices NDVI, NDRE, MSAVI, EVI and NDWI obtained from the Sentinel-2 satellite data. $SM_{f,t}^{anom,s}$ denotes the smoothed field-level soil moisture anomaly from the SMAP Level-4 product; $LST_{f,t}^{anom,s}$

denotes the smoothed land surface temperature anomaly from MODIS. Following the correlation analysis described in Section 3.1, NDVI, NDRE, and NDWI were retained as the final vegetation inputs.

Subsequently, the variables obtained in this acquired latent space were merged with meteorological data from the NASA POWER dataset. In this way, an input vector was constructed as follows to model the temporal variations of remote sensing data at the NKAES LLP:

$$X_{f,t}^{latent} = AE\left(X_{f,t}^{input}\right) = \left[Z_{1,f,t}, Z_{2,f,t}, Z_{3,f,t}\right], \quad (6)$$

where $AE(\cdot)$ represents the autoencoder component.

$$Z_{f,t} = [Z_{1,f,t}, Z_{2,f,t}, Z_{3,f,t}]$$

Finally, the latent variables were concatenated with the meteorological variables from the NASA POWER dataset to form the input to the following temporal dynamics model:

$$X_{f,t}^{model} = \left[Z_1, Z_2, Z_3, M_{f,t}\right], \quad (7)$$

And

$$M_{f,t} = [T_{f,t}, H_{f,t}, P_{f,t}, S], \quad (8)$$

where:

$T_{f,t}$—temperature,
$H_{f,t}$—humidity,
$P_{f,t}$—precipitation,
S—solar radiation.

The input features and their data sources are summarized in Table 2.

Table 2. Input features including latent representations.

Feature Group	Parameters	Source	Source Frequency	Model Frequency
Environmental (Forcing)	Temp, Precip, Humidity, Solar	NASA POWER	Daily	Monthly
Biological (Latent State)	Z_1, Z_2, Z_3	Autoencoder	Monthly (Interpolated)	Monthly

Daily NASA POWER meteorological data were aggregated to monthly values to match the temporal resolution of the latent-state variables.

The input variables were normalized to a common scale using the following Robust Scaler:

$$\tilde{X}_{f,t}^{model} = \frac{\left(X_{f,t}^{model} - median\left(X_{f,t}^{model}\right)\right)}{IQR\left(X_{f,t}^{model}\right)}, \quad (9)$$

where:

$median\left(X_{f,t}^{model}\right)$—the median value of the selected feature;
$IQR(\cdot)$—the interquartile range of the selected feature;
$\tilde{X}_{f,t}^{model}$—the standardized value of the feature.

The feature space can be modified depending on the crop under study and the growing season. The influence of highly correlated indices is reduced.

To assess sensitivity to temporal smoothing, the anomaly time series before and after Savitzky–Golay filtering were compared. The analysis included the five input variables characterizing the latent state (NDVI, NDRE, NDWI, LST, and SM). Consistency was assessed using Pearson's correlation coefficient. In this analysis, observations at the lower

and upper ends of the distribution were defined as values equal to or below the 10th percentile and equal to or above the 90th percentile, respectively. For these extreme observations, the preservation of the sign and magnitude of the anomaly after smoothing was quantitatively assessed.

The processed latent-state and climate datasets from this research are publicly available in a Zenodo repository (https://doi.org/10.5281/zenodo.23675113). The latent-state dataset was obtained by applying an autoencoder to processed Sentinel-2, MODIS, and SMAP Level-4 observations from the NKAES LLP for 2020–2025. The climate data were used as input for the time-series dynamics model.

2.5. Remote Sensing Data-Driven Framework

The digital twin framework proposed in this study is based on a monitored agroecosystem within the NKAES LLP agricultural lands. The study areas represent the physical counterpart of the digital twin.

Multisource remote sensing data are used to construct the digital latent state, representing vegetation, thermal, and water-related conditions. The latent state captures agroecosystem conditions and evolves over time as new observations become available. New remote sensing observations can be assimilated through the LAU to update the predicted latent state. In this study, this process was evaluated retrospectively under controlled observation-error conditions. The proposed «observation-prediction-assimilation-update» cycle provides a synchronized, dynamic digital representation of the agroecosystem.

Figure 3 presents the main components of the proposed framework. Multisource observations from Sentinel-2, MODIS LST, and SMAP Level 4 soil moisture are used to construct the latent state.

The MLP-AE-3D encoder maps the input variables into a three-dimensional latent representation. The decoder reconstructs the corresponding input variables. The temporal evolution of the latent state is modeled using a climate-conditioned GRU. The LAU updates the predicted latent state when new observations become available. The updated latent states are subsequently used for reconstruction and scenario-based analysis.

The architecture supports a dynamic representation of the agroecosystem state without relying on IoT devices or crop biophysical models.

The main components shown in Figure 3 were implemented and tested using historical data from 2020–2025. These include MLP-AE-3D, GRU-512, LAU/EnKF and the proposed J-RA-LAU method. Latent-state updating was evaluated retrospectively using simulated observations. The framework was also tested under various climate-stress scenarios. Integration of the validated components into the operational AgroTwin platform is underway.

Table 3 summarizes how the functional digital twin properties presented in Figure 4 are implemented and evaluated in the proposed framework. The present study evaluates the state-updating cycle retrospectively using historical Earth observation data. Integration of the proposed components into the operational AgroTwin platform is underway.

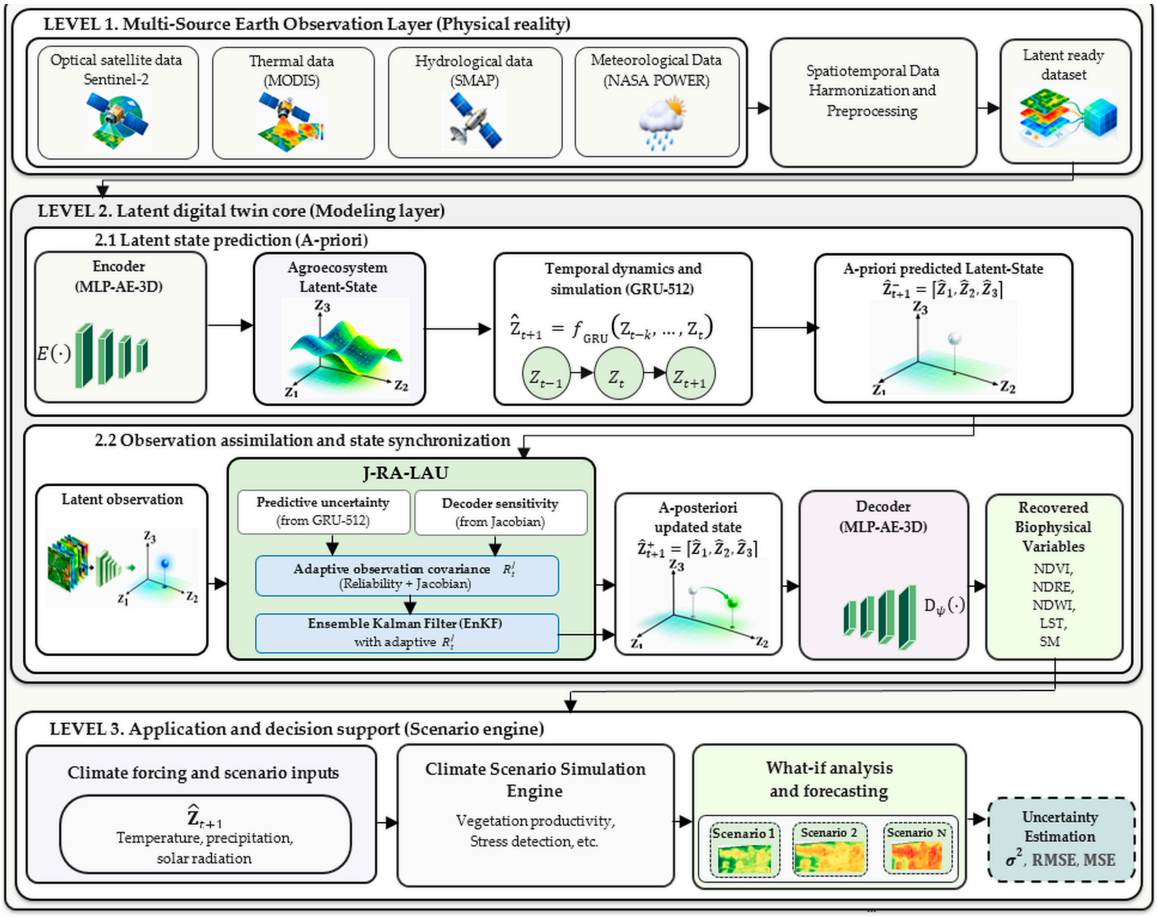


Figure 3. Remote-Sensing-Driven Agro Digital Twin Framework.

Table 3. Functional digital twin properties and additional implementation aspects of the proposed framework.

Functional Digital Twin Properties	Implementation in the Proposed Framework	Current Validation
Physical counterpart	Monitored agricultural fields	23 study fields
Observation	Multisource Earth observations	Sentinel-2, MODIS, SMAP
Digital representation	3D latent agroecosystem state	MLP-AE-3D
Dynamic state evolution	Climate-conditioned latent-state transition	GRU
Observation-driven synchronization	Predicted-state correction using new observations	LAU/EnKF
Uncertainty representation	State and observation uncertainty	EnKF covariance
What-if analysis	Climate-forcing perturbation	Scenarios
State-updating cycle	Prediction-observation-assimilation-update	Retrospectively evaluated
Real-time deployment	AgroTwin integration	In progress

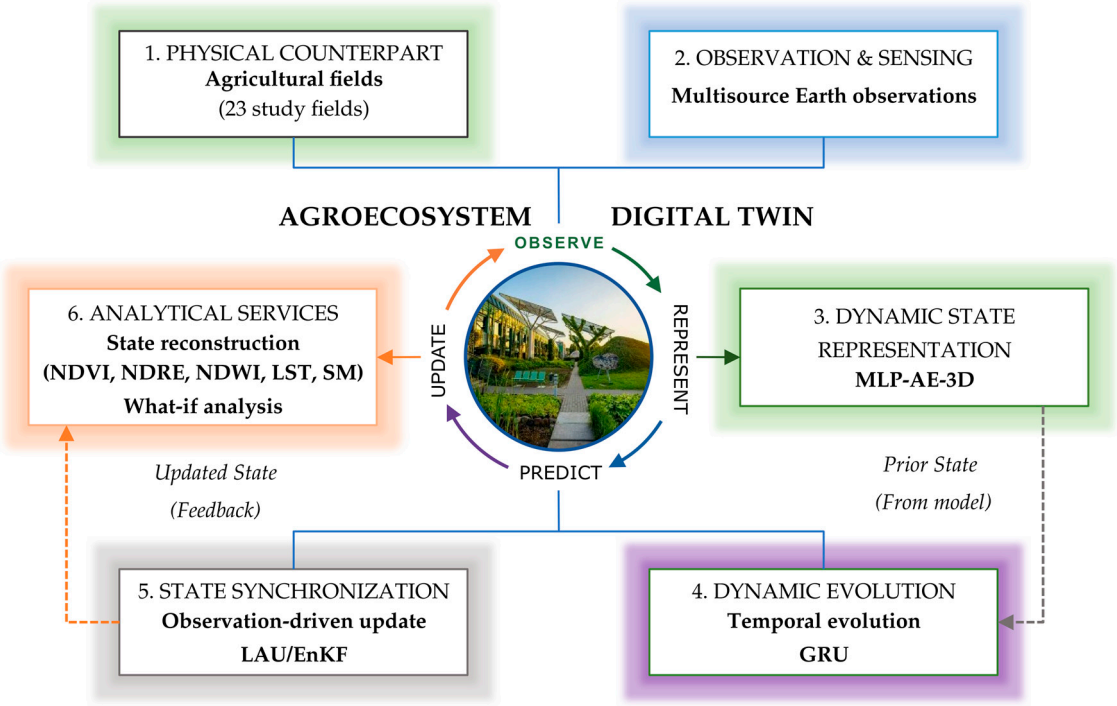


Figure 4. Functional architecture of the proposed data-driven agroecosystem digital twin.

2.5.1. Multisource Data Fusion and Feature Construction

Multisource satellite observations, including optical (Sentinel-2), thermal (MODIS LST), and hydrological (SMAP soil moisture) data, are integrated into a unified feature space. The data are preprocessed through spatial alignment, temporal compositing, and resampling, as described in Sections 2.2 and 2.4.

A set of agroecological indicators is derived, including vegetation indices (NDVI, EVI, MSAVI, NDWI, NDRE), land surface temperature (LST), and soil moisture (SM), along with their anomaly components. These variables are standardized using a Robust Scaler to ensure consistency across different scales and units.

The agroecological drivers and their corresponding anomaly-based variables used in the model are summarized in Table 4.

Table 4. Summary of agroecological drivers and their corresponding anomaly-based variables used in the model.

Driver	Variable
Vegetation condition	NDVI anomaly
Chlorophyll-related condition	NDRE anomaly
Canopy water content	NDWI anomaly
Soil moisture forcing	SM anomaly
Thermal forcing	LST anomaly

The selected variables represent key agroecological drivers that influence vegetation dynamics, water availability, and thermal stress conditions. Vegetation indices (NDVI, NDRE) capture vegetation condition and chlorophyll-related information, while NDWI and soil moisture (SM) reflect water availability. Land surface temperature (LST) is included to account for thermal stress effects.

These variables provide an integrated representation of agroecosystem conditions.

2.5.2. Latent State Encoding and Reconstruction

To represent the state of the agroecosystem, the feature space is mapped into a lower-dimensional nonlinear latent space.

$X_{f,t}^{anom,\ s} \in R^n$—denotes the normalized feature vector for field f at time t. The latent state is defined as follows:

$$Z_{f,t} = E\left(X_{f,t}^{anom,\ s}\right), Z_{f,t} \in R^d \quad (10)$$

- $E(\cdot)$—a nonlinear encoder represented as a fully connected neural network;
- $Z_{f,t}$—latent state of the agroecosystem;
- d—latent dimension of the latent space ($d = 3$);
- n—number of input features ($n = 5$).

The encoder integrates spectral, hydrological, and thermal characteristics. It reduces dimensionality and redundant information and enables the discovery of hidden relationships among the multisource data under analysis.

Instead of analyzing individual vegetation indices, the system is represented by $Z_{f,t}$ the three-dimensional latent state $Z_{f,t} = [Z_1, Z_2, Z_3]$. This representation enables dynamic modeling. The learned latent space forms the basis for the digital twin framework proposed in this study.

2.5.3. Experimental Setup

The computational experiments were conducted in Google Colab using Python (3.13.16). The main libraries included PyTorch (2.11.0+cpu), scikit-learn (1.6.1), NumPy (2.1.3), pandas (2.2.3), and SciPy (1.16.3). Geospatial processing used GEE API (1.7.39), geemap (0.38.9), GeoPandas (1.2.0), Rasterio (1.5.2), and Shapely (2.2.0). Visualization was performed using Matplotlib (3.10.0), Seaborn (0.13.2), Plotly (5.24.1), and QGIS (3.32.3).

To preserve the temporal structure of the remote sensing data for the considered agroecosystem, the dataset was divided chronologically into training (70%), validation (12%), and testing (18%) sets. Data from 2020–2023 were used for model training, data from 2024 were used for validation and hyperparameter tuning, and data from 2025 were reserved for testing. All 23 fields of the NKAES LLP were included in these datasets. This approach evaluates model performance on a later growing season and, therefore, assesses temporal generalization rather than generalization to unseen fields.

To project the NKAES data into a latent space, a linear PCA model was first fitted as a baseline. In addition, to capture nonlinear relationships in the agroecosystem, several MLP-based models were implemented: Multilayer Perceptron Autoencoders (MLP-AE), Variational Autoencoder (VMAE), VMAE-Light, temporal regularized VMAE (TR-VMAE), and physics-based regularized VMAE (PR-VMAE). To jointly examine the compactness and reconstruction quality of the obtained results, dimensions d = 2 and d = 3 were evaluated (Table 5).

Table 5. The architecture and training configuration of the autoencoders.

Parameter	Models
Models	PCA, MLP-AE, VMAE, VMAE-light, TR-VMAE, PR-VMAE
Latent dimensions	2/3
Encoder	5→128 → 64 → 32 → 16→3
Decoder	3→16 → 32 → 64 → 128 → 5
Activation	SiLU

Table 5. *Cont.*

Parameter	Models
BatchNorm	Yes
Mask ratio	0.15
Reparameterization	Yes for VMAE/TR-VMAE/PR-VMAE
Loss	MSE + βKL, plus extra regularization for TR/PR
β KL weight	0.001
Optimizer	Adam
Learning rate	1×10^{-3}
Weight decay	1×10^{-4}
Batch size	64
Epochs	300
Patience	40

Model training was performed using the Adam optimizer (learning rate = 0.001) and mean squared error (MSE) loss for 300 epochs. Before training, input features were standardized using a robust scaler to ensure numerical stability and reduce the influence of extreme values.

Both two- and three-dimensional latent configurations were evaluated, and the final configuration was selected based on reconstruction results presented in Section 3.

2.5.4. Evaluation Metrics

The framework was evaluated at four complementary levels: (i) reconstruction fidelity using R^2, MAE, and RMSE [52,53]; (ii) temporal stability of the latent representation using Seasonal Drift (SD); (iii) predictive performance of GRU-based latent-state forecasting using R^2, MAE, and RMSE; and (iv) synchronization performance by comparing the GRU prior with the LAU-updated states. This multi-level evaluation considers both representation accuracy and the dynamic behavior of the latent state as follows:

$$R^2 = 1 - \frac{\sum_f \sum_t \left(X_{f,t}^{anom,\,s} - \hat{X}_{f,t}^{anom,\,s}\right)^2}{\sum_f \sum_t \left(X_{f,t}^{anom,\,s} - \overline{X}_{f,t}^{anom,\,s}\right)^2}; \tag{11}$$

$$MAE = \frac{1}{\bar{f}t} \sum_f \sum_t \left| X_{f,t}^{anom,\,s} - \hat{X}_{f,t}^{anom,\,s} \right|; \tag{12}$$

$$RMSE = \sqrt{\sum_f \sum_t \left(X_{f,t}^{anom,\,s} - \hat{X}_{f,t}^{anom,\,s}\right)^2}, \tag{13}$$

where $X_{f,t}^{anom,\,s}$ is the observed smoothed anomalous value, and $\hat{X}_{f,t}^{anom,\,s}$ is the corresponding value reconstructed by the decoder.

The improvement from latent-state synchronization was quantified as the percentage reduction in the RMSE relative to the GRU prior as follows:

$$\Delta RMSE = \frac{RMSE_{GRU} - RMSE_{LAU}}{RMSE_{GRU}} \times 100, \tag{14}$$

where $RMSE_{GRU}$ and $RMSE_{LAU}$ denote the RMSE before and after latent-state updating, respectively.

The following Seasonal Drift (SD) metric was used to assess the temporal stability of the trained latent space; a lower SD value indicates better preservation of seasonal dynamics over time in the latent space:

$$\overline{Z}_t = \frac{1}{N_t}\sum_{t=1}^{N_t} Z_{i,t}, \tag{15}$$

$$SD = \frac{1}{T-1}\sum_{i=1}^{T-1}\left\|\overline{Z}_{t+1} - \overline{Z}_t\right\|_2, \tag{16}$$

where $\overline{Z}_t$ is the average latent state of all observations in year t, $\|\cdot\|_2$—Euclidean (L2) norm.

The framework was further evaluated through temporal forecasting, state synchronization, and the analysis of controlled climate scenarios.

2.5.5. Conditional Latent State Transition Modeling

The temporal component of the Digital Twin framework models the evolution of the agroecosystem state under climate forcing.

Let $Z_{f,t}$ denote the latent state of field f obtained from the encoder at time t. The climate-conditioned latent state transition is defined as follows:

$$\Delta Z_{f,t} = f_\theta(Z_{f,t}, C_{f,t}), \tag{17}$$

$$Z_{f,t+1} = Z_{f,t} + \Delta Z_{f,t}, \tag{18}$$

where $Z_{f,t}$ is the latent state at time t, and $Z_{f,t+1}$ is the predicted latent state at time $t+1$, $C_{f,t}$ is the climate forcing vector, $f_\theta(\cdot)$ denotes the learned temporal transition function, and θ denotes the model parameters. The climate forcing vector is defined as follows:

$$C_{f,t} = [T_{f,t,}, P_{f,t,}, H_{f,t,}, S_{f,t,}], \tag{19}$$

where:

$T_{f,t}$—air temperature;
$P_{f,t,}$ —precipitation;
$H_{f,t,}$ —humidity;
$S_{f,t,}$ —solar radiation.

Daily NASA POWER variables were aggregated to monthly values to match the temporal resolution of the latent-state sequence.

Controlled climate-stress scenarios were constructed using month-specific empirical thresholds derived from the 2020–2024 growing-season climate data. For each month from May to September, the 10th, 50th, and 90th percentiles of air temperature, precipitation, relative humidity, and solar radiation were calculated. The Heat scenario constrained air temperature to at least its monthly 90th percentile, whereas the Dry scenario constrained precipitation to at most its monthly 10th percentile. The Hot-Dry scenario combined these temperature and precipitation constraints.

The Atmospheric-Dryness scenario combined high temperature (≥90th percentile), low relative humidity (≤10th percentile), and high solar radiation (≥90th percentile). The Compound-Stress scenario additionally constrained precipitation to ≤10th percentile.

These scenarios were used as controlled sensitivity experiments rather than as projections of specific future climate pathways.

The latent core implementation and dynamic prediction flow are illustrated in Figure 5.

The latent transition is formulated as a climate-conditioned deterministic GRU mapping, in which the next latent state is predicted from the current latent state and the corresponding climate-forcing vector. Thus, "conditional" refers to using the current agroecosystem state and external drivers as inputs to the learned transition function.

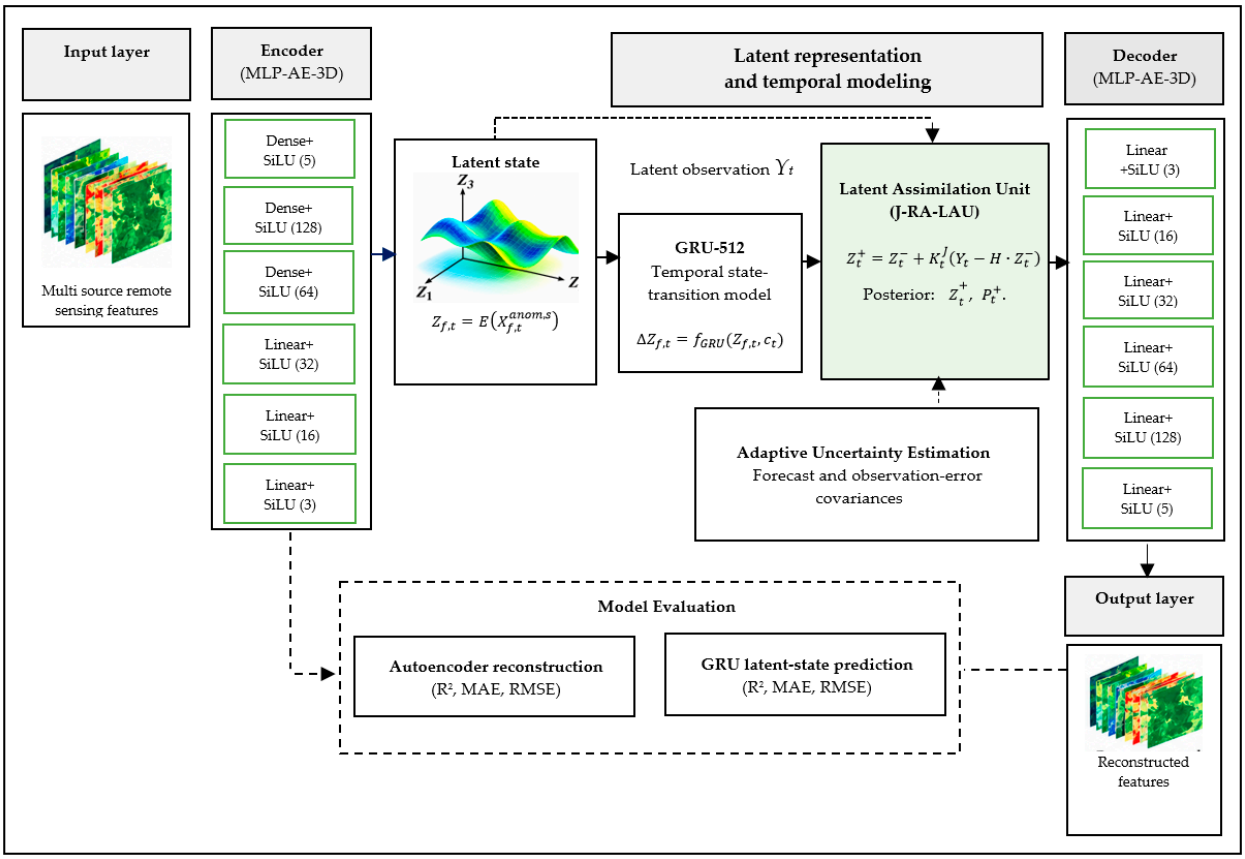


Figure 5. Latent core implementation and dynamic prediction flow.

The GRU transition itself does not define an explicit probability distribution. Probabilistic uncertainty is introduced subsequently within the LAU/EnKF state-synchronization stage through forecast and observation-error covariance.

The assimilation experiments were conducted retrospectively under a controlled observation-error setting. Synthetic latent observations were generated by adding zero-mean Gaussian noise to the held-out reference latent states, while the baseline covariance R_0 was estimated from validation-set GRU residuals. Thus, the experiment evaluates LAU, RA-LAU, and J-RA-LAU state synchronization under controlled conditions. Operational evaluation with sequential observations remains for future research.

2.5.6. Latent Data Assimilation Unit (LAU)

The Latent Data Assimilation Unit (LAU) provides the state-updating mechanism of the proposed digital twin framework. It combines the GRU-predicted latent state with a latent-space observation using an Ensemble Kalman Filter (EnKF) to obtain an updated state estimate.

Let $Z_{f,t+1}^-$ denote the latent state derived from the transition model, and $Y_{f,t+1} = E\left(X_{f,t+1}^{anom,\,s}\right)$ denotes the corresponding latent observation. Then

$$\hat{Z}_{f,\,t+1} = Z_{f,t+1}^- + K_t\left(Y_{f,t+1} - H{\cdot}Z_{f,t+1}^-\right) \tag{20}$$

The Kalman gain is defined as:

$$K_t = P_t H^T\left(HP_tH^T + R\right)^{-1} \tag{21}$$

Here, P_t denotes the forecast-error covariance matrix, R denotes the observation-error covariance matrix, H denotes the observation mapping matrix, and K_t denotes the Kalman gain matrix.

Equations (20) and (21) define the fixed-covariance LAU used as the baseline synchronization method. To account for predictive uncertainty and state-dependent uncertainty, this formulation was further extended to the adaptive variants.

For the controlled evaluation reported in this study, noisy latent observations were synthetically generated from the held-out reference states. The observation-error covariance was derived from the validation set.

The architecture of the adaptive latent-state synchronization mechanism is illustrated in Figure 6.

2.5.7. Adaptive Latent State Synchronization

The proposed Jacobian- and Reliability-Adaptive Latent-State Synchronization (J-RA-LAU) mechanism is summarized in Algorithm 1.

Algorithm 1. J-RA-LAU Latent State Synchronization

Input: GRU latent-state ensemble $\{Z_t^{-(m)}\}_{m=1}^{M}$, latent observation Y_t, baseline observation-error covariance R_0, validation-derived normalization statistics, decoder-sensitivity statistics, frozen MLP-AE-3D decoder $D(\cdot)$, adaption parameters α and β.
Output: synchronized posterior latent state Z_t^+ and posterior covariance P_t^+.

Step 1. Prior-state estimation
Estimate the a priori latent state and its uncertainty from the GRU-512 ensemble:

$$Z_t^- = \frac{1}{M}\sum_{m=1}^{M} Z_t^{-(m)}, \tag{22}$$

$$P_t^- = Cov\left(Z_t^{-(1)}, \ldots, Z_t^{-(M)}\right). \tag{23}$$

Step 2. Reliability adaptation:
Adjust the observation-error covariance according to GRU-512 predictive uncertainty:

$$R_{j,t}^{RA} = \frac{R_{0,j}}{1 + \alpha u_{j,t}}, \tag{24}$$

Step 3. Decoder-sensitivity adaptation:
Estimate the sensitivity of each latent dimension using the frozen decoder:

$$J_t = \left|\frac{\partial D(Z)}{\partial Z}\right|_{Z=Z_t}, \tag{25}$$

$$s_{j,t} = \left\|J_{j,t}\right\|_2. \tag{26}$$

Normalize $s_{j,t}$ to obtain moderator $g_{j,t} \in [-1, 1]$ and define:

$$R_{j,t}^{JRA} = R_{j,t}^{RA}\left(1 + \beta g_{j,t}\right), \tag{27}$$

Step 4. Latent state update:
Calculate the adaptive Kalman gain and update the predicted latent state:

$$K_{j,t}^{J} = P_t^- H^T\left(HP_t^- H^T + R_{j,t}^{JRA}\right)^{-1} \tag{28}$$

$$Z_t^+ = Z_t^- + K_t^J(Y_t - H{\cdot}Z_t^-), \quad H = I_3, \tag{29}$$

$$P_t^+ = \left(I - K_t^J H\right)P_t^-. \tag{30}$$

Return: Z_t^+, P_t^+.

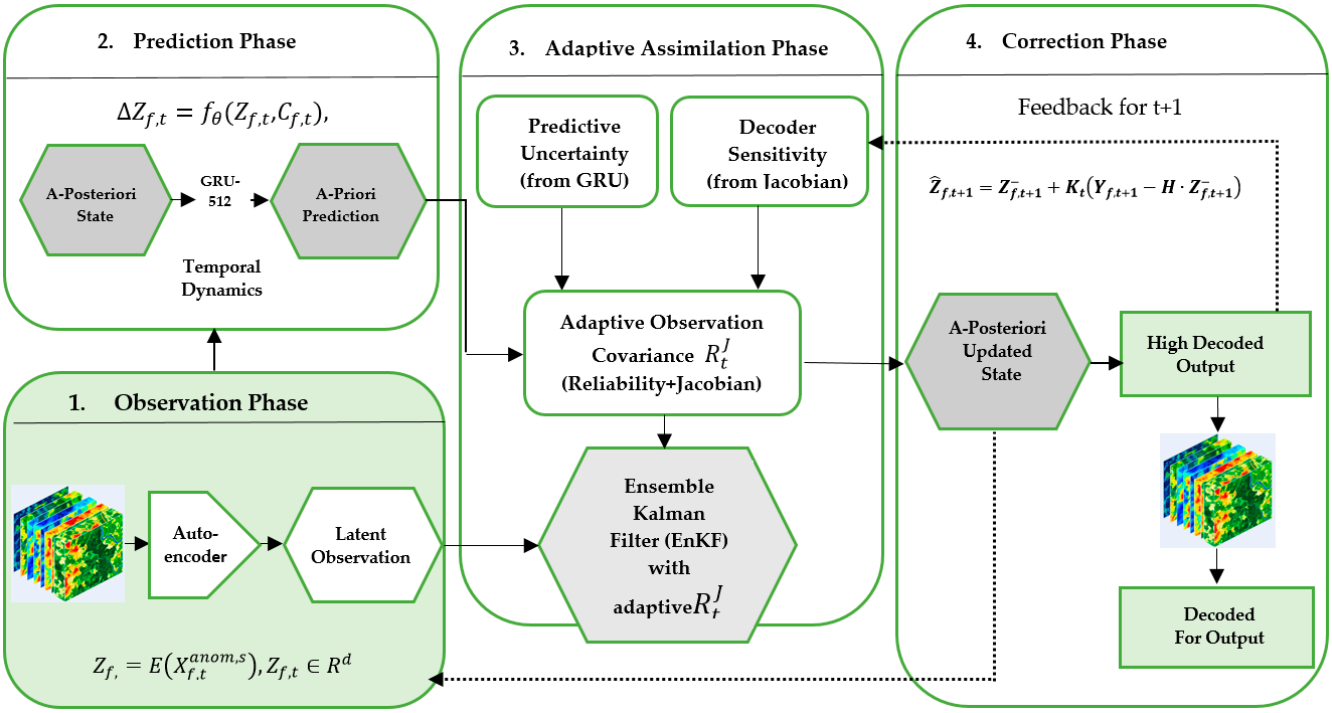


Figure 6. The architecture of the adaptive latent state synchronization mechanism within the proposed Digital Twin framework.

In the proposed algorithm, adaptation parameters were selected using a validation set. The reliability confidence coefficient was set to $\alpha = 0.5$ based on a prior validation experiment. To determine decoder sensitivity, $\beta = \{0.1, 0.2, 0.3\}$ were evaluated on the validation set, and $\beta = 0.3$ was selected based on the lowest RMSE. No parameter tuning was performed on the test set.

2.5.8. Scenario-Based Simulation

To investigate the response of the latent agroecosystem state in the NKAES fields to weather-related stress, five controlled scenarios were developed to assess sensitivity. The growing season from May to September during 2020–2024 was used to derive the scenario thresholds. Heat stress was based on the monthly 90th percentile (P90) of air temperature, and precipitation deficit was based on the 10th percentile (P10) of positive precipitation values. Atmospheric dryness was determined by the P10 of humidity and the P90 of solar radiation. Only variables that had not already exceeded their respective stress thresholds were modified. The baseline scenario retained observed climatic inputs.

The controlled climate-stress scenarios are summarized in Table 6.

These scenarios were used as controlled sensitivity experiments rather than as projections of specific future climate pathways.

For each scenario, the climate-conditioned GRU-512 was used to predict the subsequent latent state as described in Section 2.5.5. The predicted latent state was then mapped back to the observation space using the following decoder:

$$\hat{X}_{f,t+1}^{anom,s} = D\left(\hat{Z}_{f,t+1}\right), \quad (31)$$

where $D(\cdot)$ denotes the decoder network, and $\hat{X}_{f,t+1}^{anom,\,s}$ denotes the reconstructed anomaly feature vector.

Table 6. Controlled climate-stress sensitivity scenarios applied to the GRU-based latent-state simulation.

Scenario	Temperature (°C)	Precipitation	Humidity	Solar Radiation
Baseline	Observed	Observed	Observed	Observed
Heat	≥monthly P90	Observed	Observed	Observed
Dry	Observed	≤monthly P10 of positive precipitation	Observed	Observed
Hot-Dry	≥monthly P90	≤monthly P10 of positive precipitation	Observed	Observed
Atmospheric-Dryness	≥monthly P90	Observed	≤monthly P10	≥monthly P90
Compound-Stress	≥monthly P90	≤monthly P10 of positive precipitation	≤monthly P10	≥monthly P90

3. Results and Discussion

The proposed Digital Twin framework was evaluated according to the main methodological stages described in Section 2. The results include feature analysis, latent-state representation, temporal prediction, state synchronization, and scenario-based analysis.

3.1. Feature Preparation and Correlation Analysis

Remote sensing data for the 2020–2025 growing seasons were preprocessed as described in Section 2.3 and used to construct the latent-state input dataset. Monthly anomalies were calculated to represent deviations from typical seasonal conditions. Savitzky–Golay smoothing was applied using a window length of 5 and a second-order polynomial.

To examine relationships among the initial variables, a correlation analysis was conducted. Strong correlations were observed among the NDVI, EVI, and MSAVI anomaly values ($r = 0.96$–0.98). This indicates substantial overlap among these vegetation indices. In contrast, the NDWI index demonstrated a negative correlation with the other vegetation indices. This suggests that this index provides additional information on canopy water status.

The LST variable showed a weak correlation with vegetation indices. Soil moisture showed a moderate negative correlation with LST ($r = -0.47$). This suggests that these variables provide additional information on thermal and hydrological conditions.

The correlations among the selected remote sensing variables are summarized in Figure 7.

Based on these results, anomalous values of key variables such as vegetation condition, chlorophyll level, leaf water content, heat stress, and soil moisture were selected.

$$\boldsymbol{X}_{f,t}^{anom,s} = \left[\boldsymbol{NDVI}_{f,t}^{anom,s}, \boldsymbol{NDRE}_{f,t}^{anom,s}, \boldsymbol{NDWI}_{f,t}^{anom,s}, \boldsymbol{LST}_{f,t}^{anom,s}, \boldsymbol{SM}_{f,t}^{anom,s} \right] \quad (32)$$

NDVI, MSAVI, and NDRE were strongly correlated (r = 0.96–0.98). This suggests that these indices capture similar vegetation-related information. MSAVI was excluded because of its high redundancy with NDVI and NDRE. NDVI was retained as a general indicator of vegetation condition, while NDRE preserved red-edge information related to chlorophyll status [54]. Accordingly, NDVI, NDRE, NDWI, LST, and SM were selected as the final latent-state inputs.

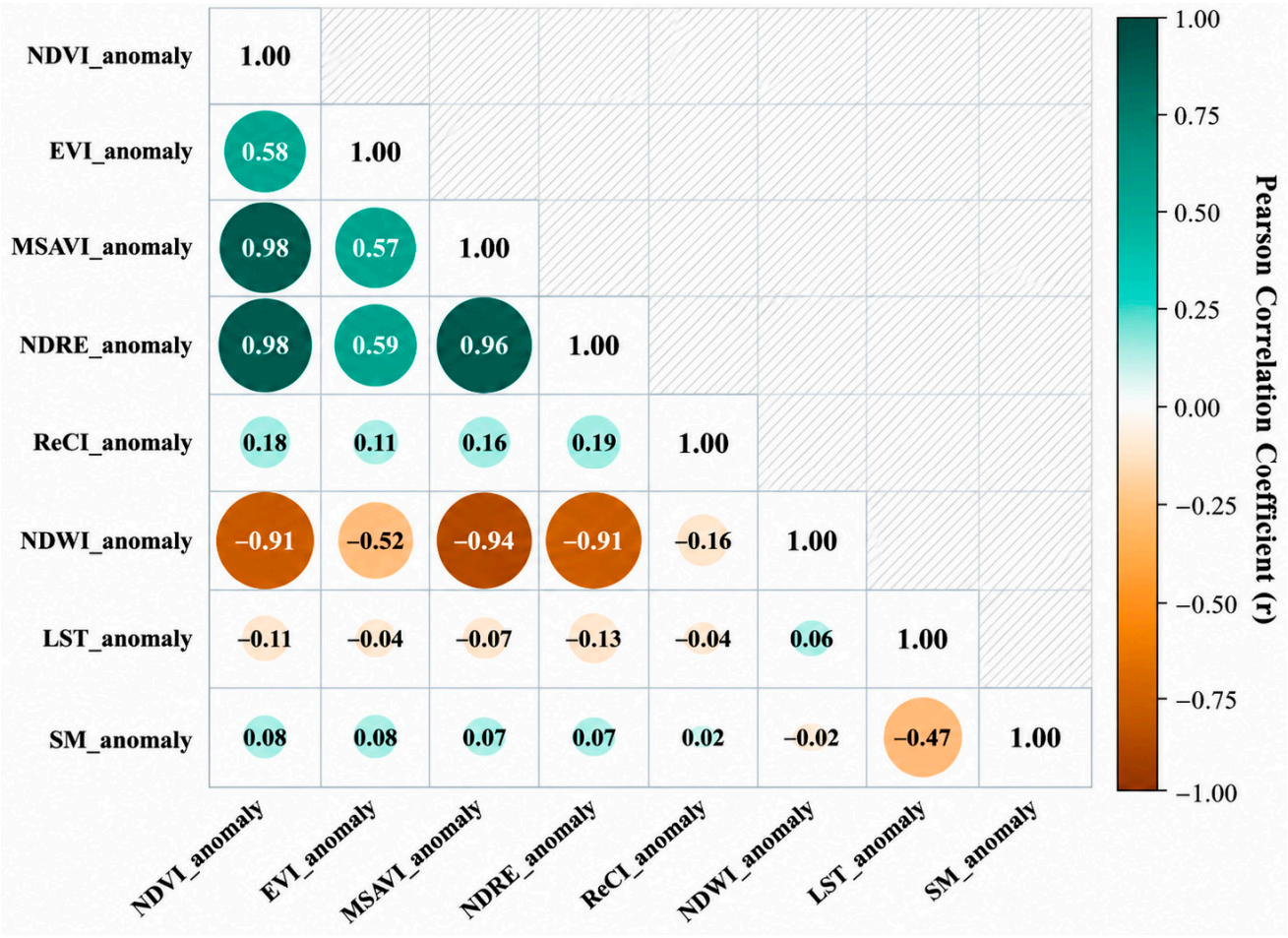


Figure 7. Correlation matrix of candidate remote sensing variables for the study region during 2020–2025.

3.2. Comparative Evaluation of Latent Representation Models

After selecting the agroecosystem variables, a compact latent space was constructed from these variables. For this purpose, PCA was first considered as the linear baseline. For comparison, several nonlinear autoencoder models were trained in two- and three-dimensional latent spaces.

The agroecosystem under consideration is a complex multisource system. This includes the traditional MLP-AE, VMAE, and its simplified version VMAE-Light, as well as the temporally regularized TR-VMAE models in two- and three-dimensional latent spaces. The physics-based PR-VMAE model was evaluated by incorporating physical constraints.

The results are presented in Table 7.

For several evaluated models, three-dimensional latent representations generally provided better reconstruction performance than their two-dimensional counterparts. Among the nonlinear autoencoders, MLP-AE-3D provided a favorable balance between reconstruction performance and seasonal stability. It achieved Val $R^2 = 0.9554$ and Test $R^2 = 0.9654$. The corresponding Val and Test RMSE values were 0.243 and 0.210. Its Seasonal Drift (SD) value was 0.2209, the lowest among the evaluated three-dimensional nonlinear autoencoder models.

PCA-3D achieved higher reconstruction accuracy. However, MLP-AE-3D showed high reconstruction accuracy and substantially lower seasonal drift and was therefore selected as the final nonlinear latent representation. The lower SD value indicates greater seasonal stability of the MLP-AE-3D latent representation.

Table 7. Performance metrics of latent-space reconstruction models.

Model	Latent Dim	Val R^2	Test R^2	Val RMSE	Test RMSE	SD (Seasonal Drift)
PCA-2D (Baseline)	2	0.7746	0.8910	0.5053	0.3162	0.6803
MLP-AE-2D	2	0.8034	0.8650	0.4720	0.3519	0.6946
VMAE-128-64-32-2D	2	0.8018	0.8804	0.4739	0.3313	0.9573
VMAE-Light-2D	2	0.7913	0.8484	0.4863	0.3730	1.1251
TR-VMAE-2D	2	0.9415	0.8967	0.4995	0.3631	0.5152
PI-VMAE-2D	2	0.8920	0.8538	0.4600	0.3427	0.8496
PR-VMAE-2D	2	0.7968	0.3665	0.3996	0.2632	0.4153
PCA-3D	3	0.9777	0.9800	0.1720	0.1600	0.9766
MLP-AE-3D	3	0.9554	0.9654	0.2430	0.2101	0.2209
VMAE-128-64-32-3D	3	0.9216	0.9594	0.3222	0.2278	0.6224
VMAE-Light-3D	3	0.9315	0.9591	0.3013	0.2287	0.9793
PR-VMAE-3D	3	0.9415	0.9599	0.2783	0.2264	0.7177
PI-VMAE-3D	3	0.9020	0.9538	0.3600	0.2427	0.9496
TR-VMAE-3D	3	0.8968	0.2665	0.4996	0.3632	0.5153

To further evaluate the robustness of the proposed preprocessing pipeline, an additional temporal smoothing sensitivity analysis was performed. The analysis showed a strong correlation between smoothed and unsmoothed vegetation indices (r = 0.8775–0.971). For observations in the lower and upper tails, anomaly-sign agreement ranged from 98.55% to 100%. Anomaly-magnitude preservation ranged from 72.35% to 77.83% and from 64.76% to 101.46% for the lower and upper tails, respectively (Table S1).

3.3. Sensitivity to Coarse-Resolution Spatial Harmonization

To determine whether the learned latent representation was affected by coarse-resolution inputs, a spatial-sensitivity analysis was performed. The results showed that resampled MODIS LST and SMAP SM values aggregated to field-year-month means had correlations of 0.999998 and 0.999997, respectively.

The sample sizes in Table 8 were determined from the processed pixel-level datasets. For LST and SM, n = 18,259,050 corresponds to 608,635 spatial pixels across 30 months. For the latent states Z_1, Z_2, and Z_3, the 30 monthly latent-state files contained 17,572,964 records in total. The smaller latent-state sample reflects data-quality filtering. Latent representations were generated only for records with finite values across all five smoothed input features (NDVI, NDRE, NDWI, LST and SM anomalies).

Table 8. Sensitivity of coarse-resolution inputs and latent states to spatial aggregation.

Variable	*n*	MAE	RMSE	$\sigma_{original}$	NRMSE (%)	Correlation
LST	18,259,050	0.005159	0.007328	3.754188	0.195	0.999998
SM	18,259,050	0.000073	0.000101	0.041080	0.245	0.999997
Z_1	17,572,964	0.000304	0.000419	0.228294	0.187	0.999998
Z_2	17,572,964	0.000234	0.000358	0.15262	0.237	0.999997
Z_3	17,572,964	0.000132	0.000193	0.169010	0.116	0.999999

Note: *n* denotes the number of pixel-month records included in the analysis.

Figure 8 shows the effect of spatial harmonization at the observation level. The original and sensitivity-derived latent states were closely aligned across all three latent dimensions. The residual differences were centered near zero. The NRMSEs were 0.187% for Z_1, 0.237% for Z_2, and 0.116% for Z_3. These results indicate only minor differences between the original and sensitivity-derived latent states.

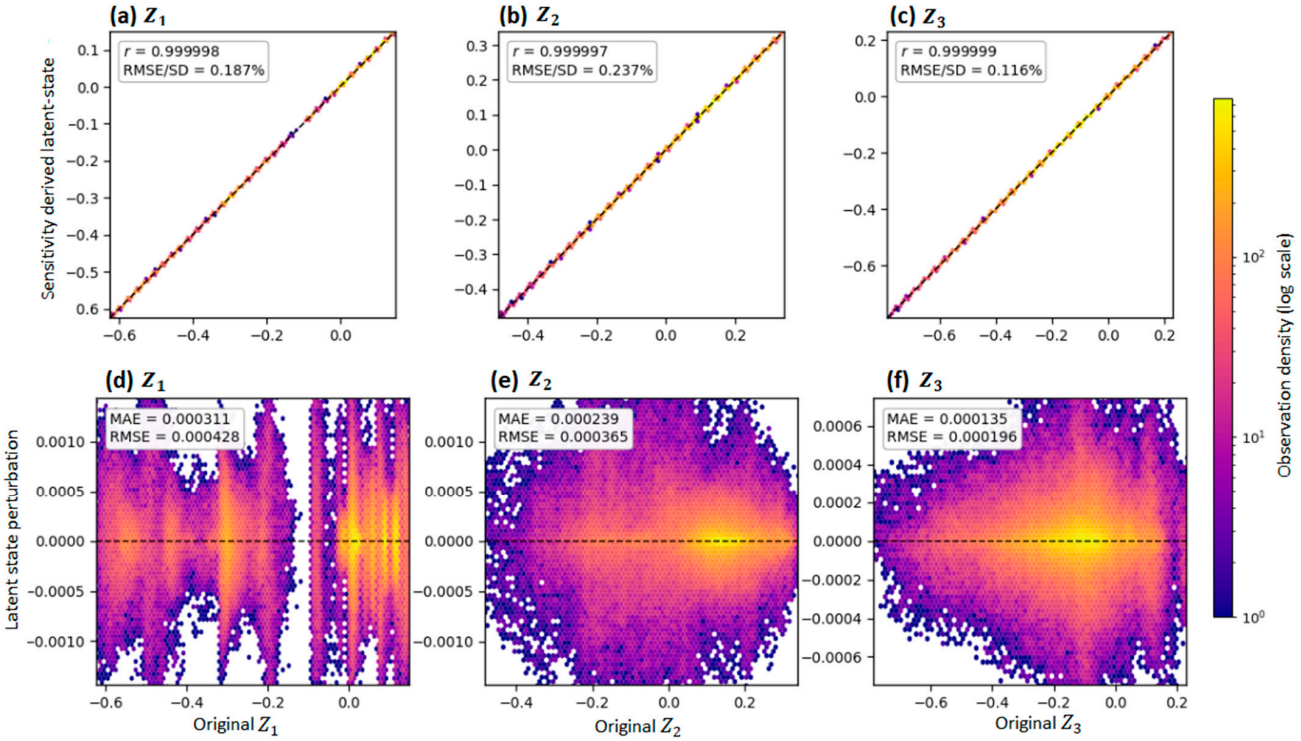


Figure 8. Sensitivity of the learned latent representation to spatial harmonization of coarse-resolution inputs.

Based on the reconstruction and seasonal-stability results, MLP-AE-3D was selected as the latent-state encoder for the subsequent analyses.

Reconstruction performance was high across the five selected variables, with R^2 values from 0.872 for NDWI to 0.973 for SM.

The reconstruction performance of the MLP-AE-3D model for the selected anomaly variables is illustrated in Figure 9.

3.4. Latent Space Interpretation

To interpret the learned latent space, correlations between the input variables and the resulting latent-state components were calculated (Figure 10).

The Z_1 latent component showed a strong positive correlation with LST (r = 0.96) and a negative correlation with SM (r = −0.67). This suggests that the Z_1 primarily captures thermal and moisture-related variations.

The second latent component, Z_2, showed moderate positive correlations with the NDVI and NDRE (r = 0.61 and r = 0.62, respectively). It also showed negative correlations with NDWI (r = −0.65) and SM (r = −0.62). This suggests that Z_2 captures variations related to vegetation and moisture conditions.

The third latent component, Z_3, showed a strong positive correlation with NDWI (r = 0.88). However, it also showed strong negative correlations with NDVI (r = −0.93) and NDRE (r = −0.92). Thus, Z_3 primarily represents a contrast between vegetation greenness/red-edge response and canopy moisture.

Thus, these three latent components provide a compact representation of thermal, hydrological, and vegetation-related variations, as summarized in Table 9.

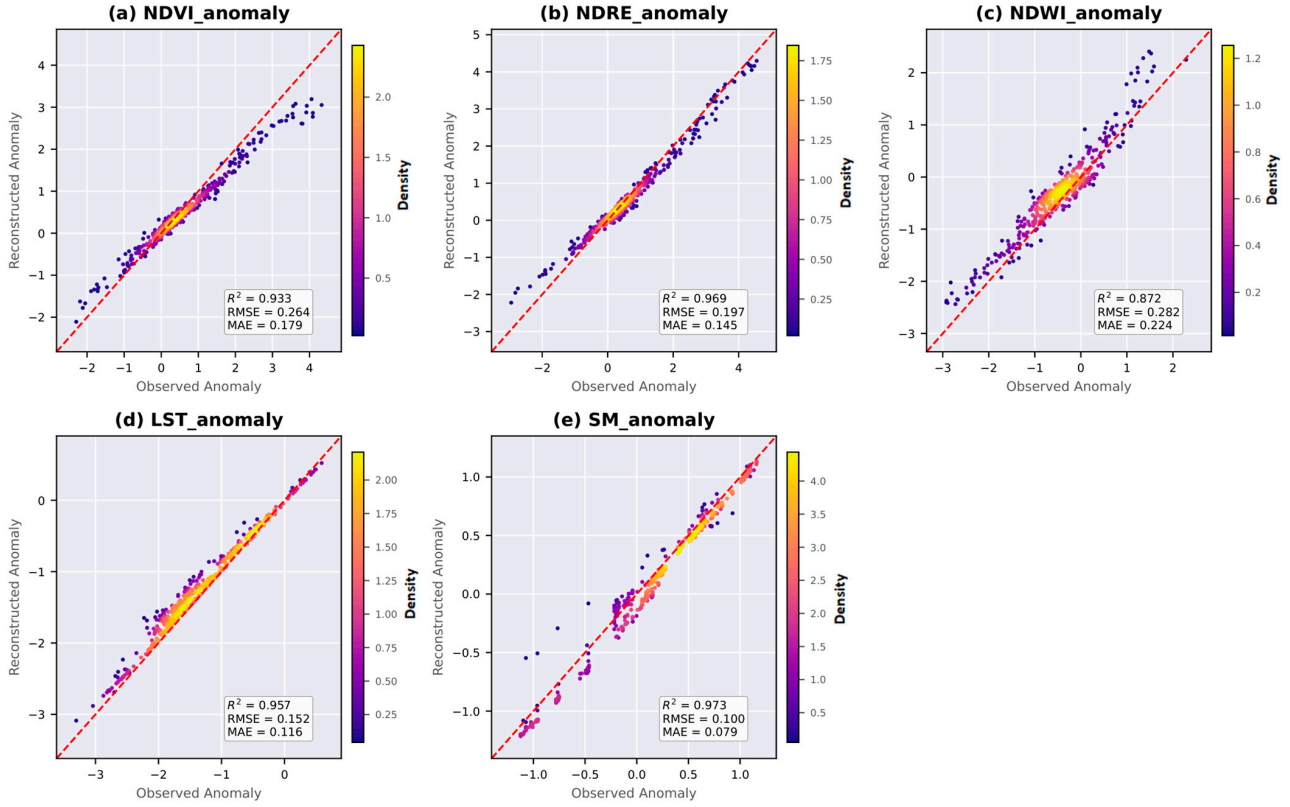


Figure 9. Reconstruction performance of the MLP-AE-3D model for the selected anomaly variables.

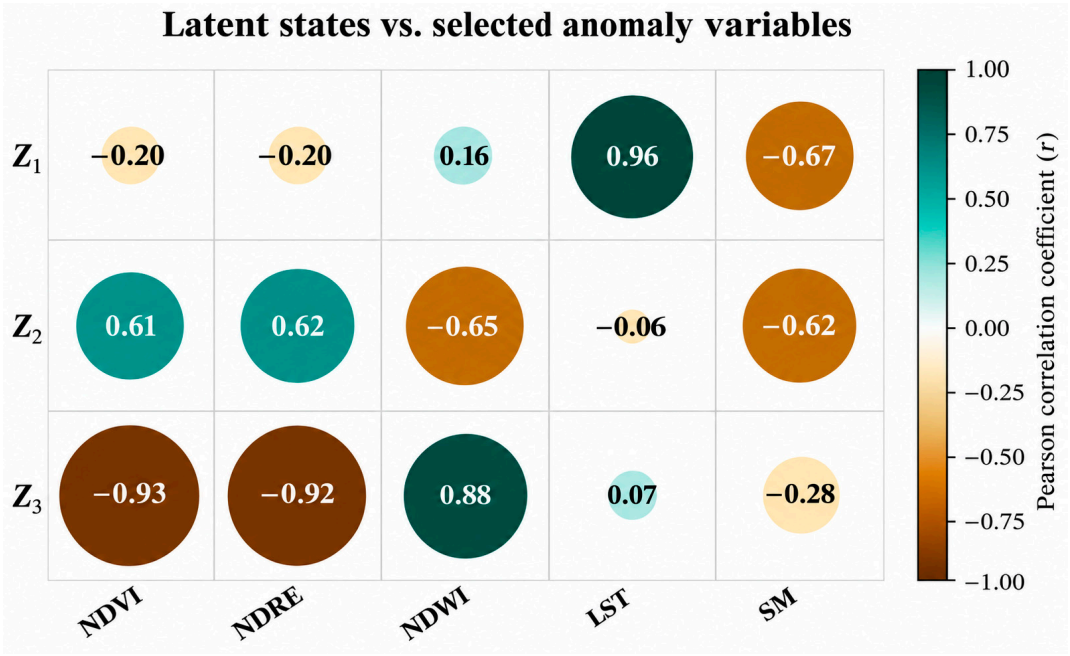


Figure 10. Correlation matrix between latent states and selected anomaly variables.

Table 9. Agronomic interpretation of the learned latent components.

Latent State	Dominant Variable	Correlation	Interpretation
Z_1	LST	0.96	Thermal and moisture stress
Z_2	NDVI, NDRE	0.61–0.62	Vegetation-moisture variation
Z_3	NDWI	0.88	Vegetation-moisture contrast

Based on these relationships, the three latent components were interpreted as thermal and moisture variation (Z_1), vegetation-moisture variation (Z_2), and vegetation moisture contrast (Z_3).

To provide a field-level qualitative example of the learned latent-state dynamics, the seasonal evolution of the three latent dimensions was examined for Field 17.

Figure 11 illustrates the seasonal patterns of the three latent dimensions Z_1, Z_2, and Z_3.

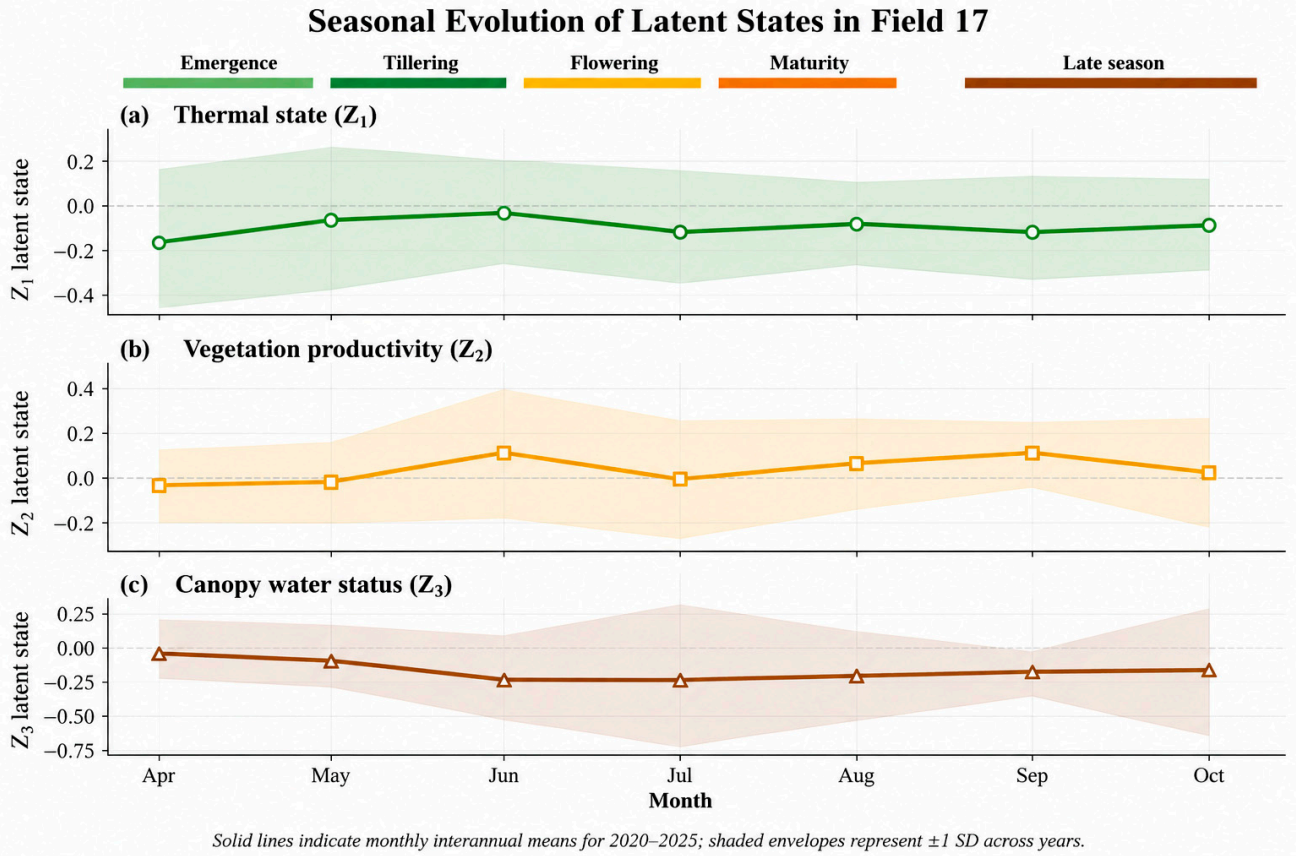


Figure 11. Seasonal dynamics and variability of the learned latent states in Field 17 during 2020−2025.

The latent dimensions show distinct seasonal changes across the growing season. The shaded envelopes indicate interannual variability. These field-level trajectories provide a qualitative view of the seasonal behavior of the learned latent dimensions.

To further evaluate the structure of the learned latent space, the distribution of the agroecosystem states was compared with that obtained using the traditional linear component method. Figure 12 shows the data projections obtained using PCA and the proposed MLP-AE-3D model. Figure 12b shows the distribution of the agroecological states in the nonlinear latent space. The results show a compact and structured latent manifold.

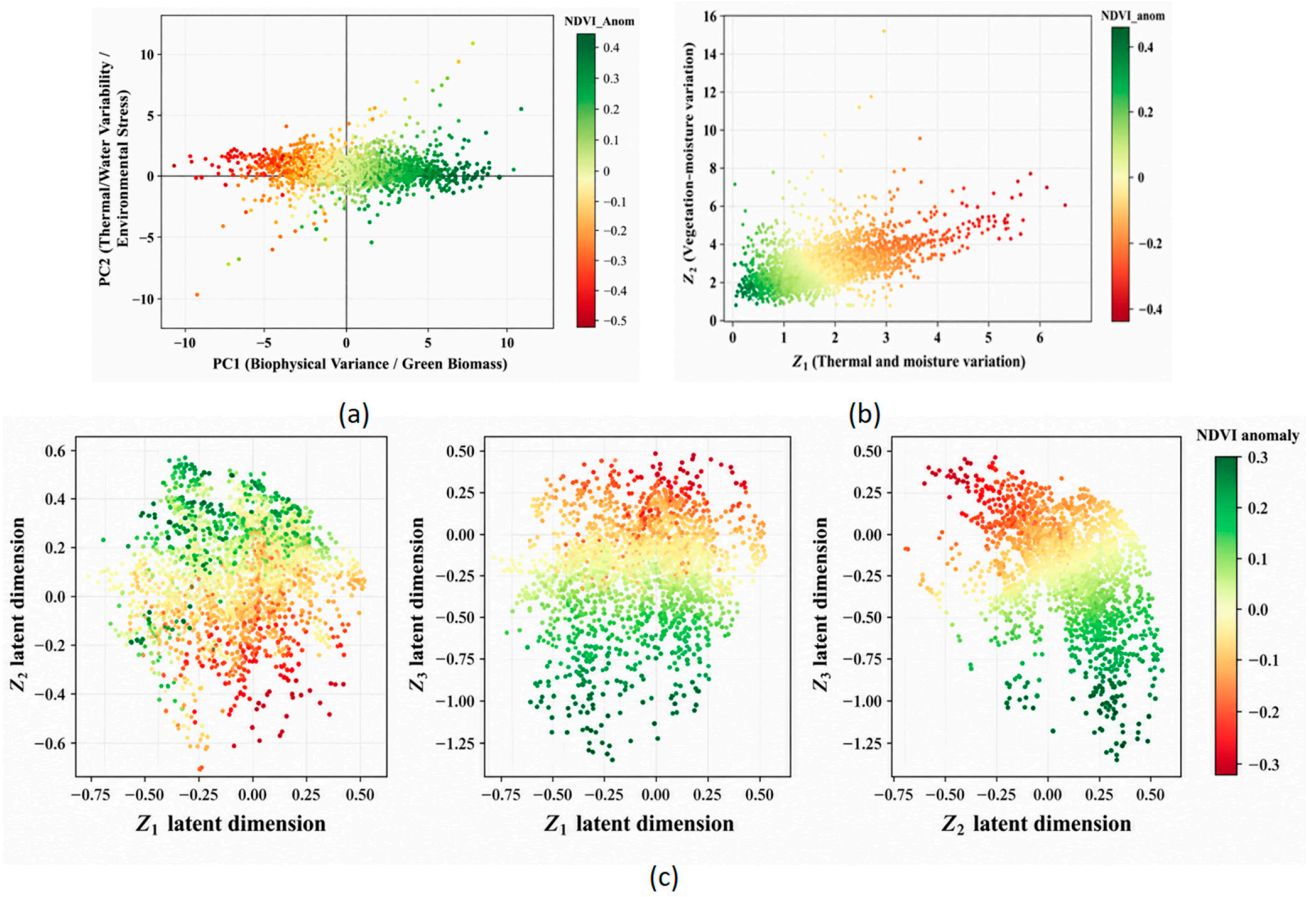


Figure 12. Comparison of linear and nonlinear latent representations of the agroecosystem state. (**a**) PCA projection of the NDVI anomalies; (**b**) MLP-AE-3D projection of the NDVI anomalies; (**c**) three pairwise projections of the MLP-AE-3D space.

As shown in Figure 12a, the linear PCA projection preserves the dominant dispersion structure in the anomaly indices of the agroecosystem under consideration.

In Figure 12b, the MLP-AE-3D model provides an alternative nonlinear representation of the agroecosystem states.

Figure 12c shows pairwise projections of the three-dimensional latent space obtained using the MLP-AE-3D model.

To provide a clearer visualization, the relationships among the Z_1, Z_2, and Z_3 latent components are shown separately. The pairwise projections show structured variations across the three latent components.

The quantitative evaluation metrics of the MLP-AE-3D model also demonstrated good performance. The reconstruction performance was Test $R^2 = 0.9654$, and the seasonal drift was SD = 0.2209. These results indicate low seasonal drift in the learned latent representation.

3.5. Dynamic Latent State Evolution Within the Digital Twin Framework

To model temporal agroecosystem dynamics, three temporal models with different structures were evaluated. The multilayer perceptron (MLP) served as a nonlinear baseline model. The Gated Recurrent Unit (GRU) and Temporal Scenario Network (TSN) models were used to capture complex temporal changes. These models were used to characterize latent-state evolution over 150 steps. To assess model performance, the models were trained and evaluated using hidden dimensions of 128, 256, and 512.

As shown in Table 10, among the evaluated models, the GRU model with a hidden dimension of 512 achieved the highest R^2 (0.7962 ± 0.0237) and the lowest Test MAE (0.0517 ± 0.0042) and Test RMSE (0.0749 ± 0.0041).

Table 10. Quantitative performance comparison of models for latent state prediction.

Model	Model Function	Hidden	Train R^2	Val R^2	Test R^2	Test MAE	Test RMSE
MLP	Baseline	128	0.9039 ± 0.0187	0.8472 ± 0.0064	0.7250 ± 0.0243	0.0573 ± 0.0015	0.0870 ± 0.0038
		256	0.9071 ± 0.0165	0.8458 ± 0.0066	0.7374 ± 0.0142	0.0563 ± 0.0015	0.0850 ± 0.0023
		512	0.9023 ± 0.0157	0.8471 ± 0.0024	0.7186 ± 0.0339	0.0580 ± 0.0023	0.0879 ± 0.0052
GRU	State-transition	128	0.8940 ± 0.0277	0.8334 ± 0.0078	0.7518 ± 0.0087	0.0569 ± 0.0016	0.0827 ± 0.0014
		256	0.8999 ± 0.0452	0.8439 ± 0.0218	0.7702 ± 0.0153	0.0552 ± 0.0023	0.0795 ± 0.0027
		512	0.9168 ± 0.0463	0.8511 ± 0.0167	0.7962 ± 0.0237	0.0517 ± 0.0042	0.0749 ± 0.0041
TSN	Alternative-temporal	128	0.9166 ± 0.0365	0.8276 ± 0.0076	0.7505 ± 0.0130	0.0571 ± 0.0022	0.0829 ± 0.0022
		256	0.9406 ± 0.0465	0.8376 ± 0.0091	0.7333 ± 0.0189	0.0574 ± 0.0025	0.0857 ± 0.0030
		512	0.9485 ± 0.0211	0.8432 ± 0.0132	0.7425 ± 0.0207	0.0564 ± 0.0017	0.0842 ± 0.0034

Figure 13 illustrates the distributions of the predicted residuals for the MLP, GRU, and TSN models with a hidden dimension of 512 on the independent test set.

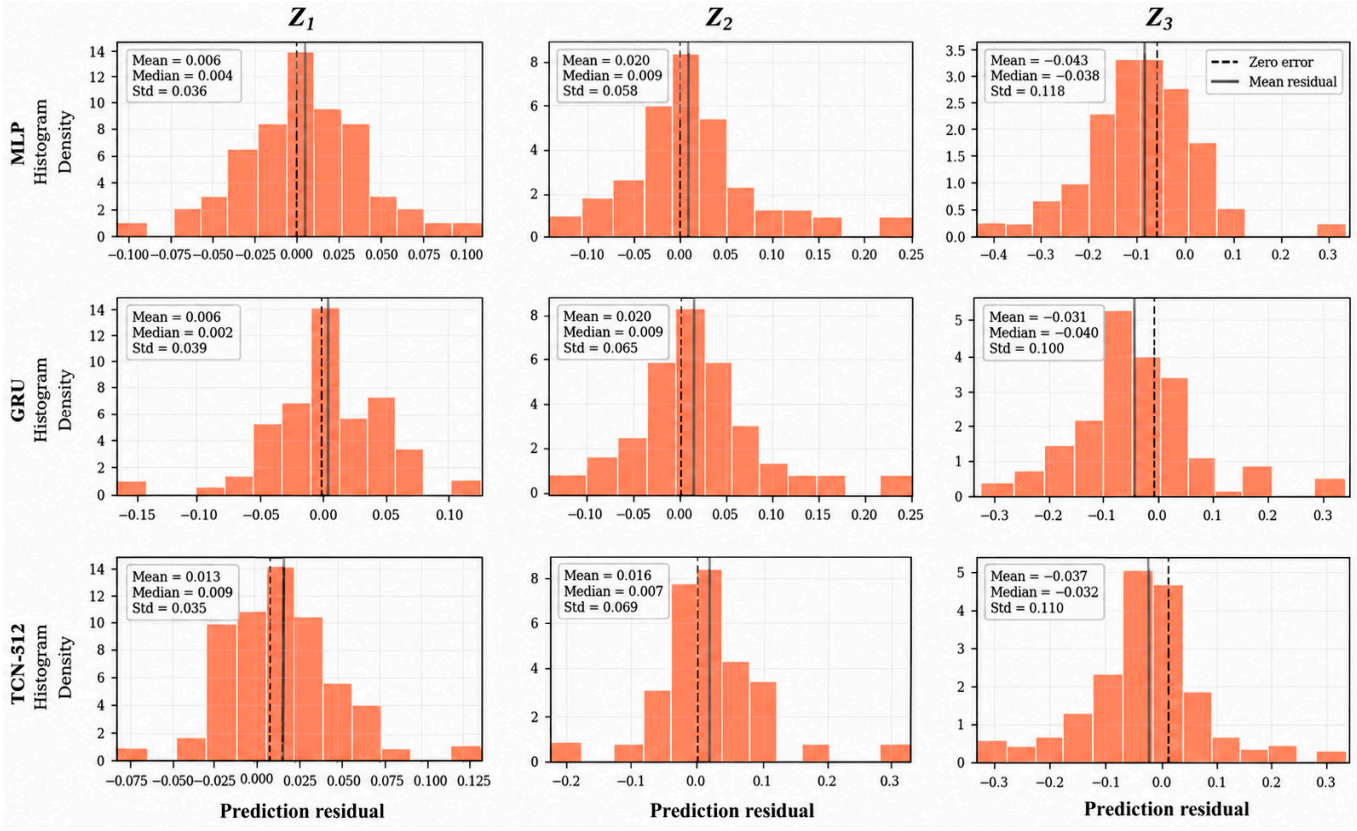


Figure 13. Residual distributions of predicted latent states for three neural network models.

Although the TSN model had higher R^2 values on the training set, its validation was lower than that of the GRU model. Based on these results, GRU-512 was selected as the temporal state-transition model.

Figure 14 presents the prediction performance of the selected GRU model. This figure shows the prediction performance of the GRU-512 model on the independent test set.

Figure 14a shows the prediction results, with $R^2 = 0.796$, MAE = 0.052, and RMSE = 0.075. The predicted and observed latent states showed good agreement. The Z1 variable achieved the best prediction performance ($R^2 = 0.95$, MAE = 0.029, RMSE = 0.040). The R^2 values were 0.75 for predicting Z_2 and 0.45 for predicting Z_3. Thus, these results indicate that Z_3 had higher prediction errors than Z1 and Z2.

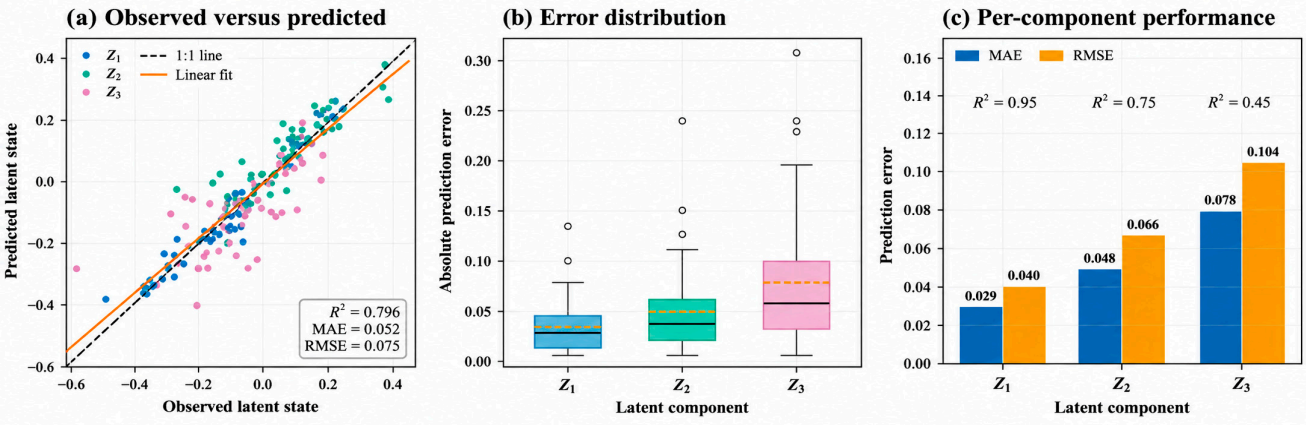


Figure 14. Held-out test performance of the GRU-512 latent residual dynamics model: (**a**) observed versus predicted latent variables (colored points: observed-predicted pairs; dashed line: 1:1 reference; solid line: linear fit); (**b**) absolute prediction error distribution (boxes: interquartile ranges; solid center lines: medians; dashed lines: means; whiskers: non-outlier data ranges; circles: outliers); (**c**) per-component performance (MAE, RMSE, and R^2).

3.6. Evaluation of Digital Twin State Synchronization

The proposed framework was also evaluated for latent-state synchronization. The GRU-512 output was used as the prior latent state. Noisy latent observations were synthetically generated from the held-out reference states and assimilated using LAU.

This produced a posterior latent state. The updated states were compared with the observation-derived latent states to evaluate state synchronization.

The assimilation results for the GRU-512 model are presented in Table 11.

Table 11. Effect of the Latent Assimilation Unit on GRU-512 latent state estimation.

Latent Component	Prior R^2	Assimilated R^2	Prior MAE	Assimilated MAE	Prior RMSE	Assimilated RMSE	RMSE Reduction
Z_1	0.9539	0.9722	0.0292	0.0229	0.0400	0.0311	22.25%
Z_2	0.7541	0.7664	0.0476	0.0448	0.0659	0.0642	2.53%
Z_3	0.4508	0.4794	0.0783	0.0771	0.1044	0.1017	2.63%
Overall	0.7962	0.8133	0.0517	0.0483	0.0749	0.0717	4.29%

As demonstrated in Table 11, the assimilation using the LAU improved the overall R^2 from 0.7962 to 0.8133 and reduced the RMSE from 0.0749 to 0.0717. The posterior covariance trace was approximately 44% lower than the prior covariance trace. This indicates reduced latent-state uncertainty after LAU assimilation under the controlled evaluation setting.

The observation-error covariance matrix R was estimated from the validation set. Table 12 presents the standard deviations and observation-error variances of the latent components.

Table 12. Observation covariance estimated from the validation set.

Latent Component	Observation σ	Observation Variance (R)
Z_1	0.03328	0.00111
Z_2	0.05714	0.00326
Z_3	0.12358	0.01527

As can be seen, the observation uncertainty differed among the three components. The lowest standard deviation was observed for Z_1 (0.03328) and the highest for Z_3 (0.12358). These values were applied in the EnKF through the observation-error covariance matrix.

Figure 15 shows the effect of LAU on latent-state synchronization. The posterior uncertainty was generally lower than the prior uncertainty. The latent-state error also decreased after assimilation. These results support the state-synchronization function of the proposed digital twin framework.

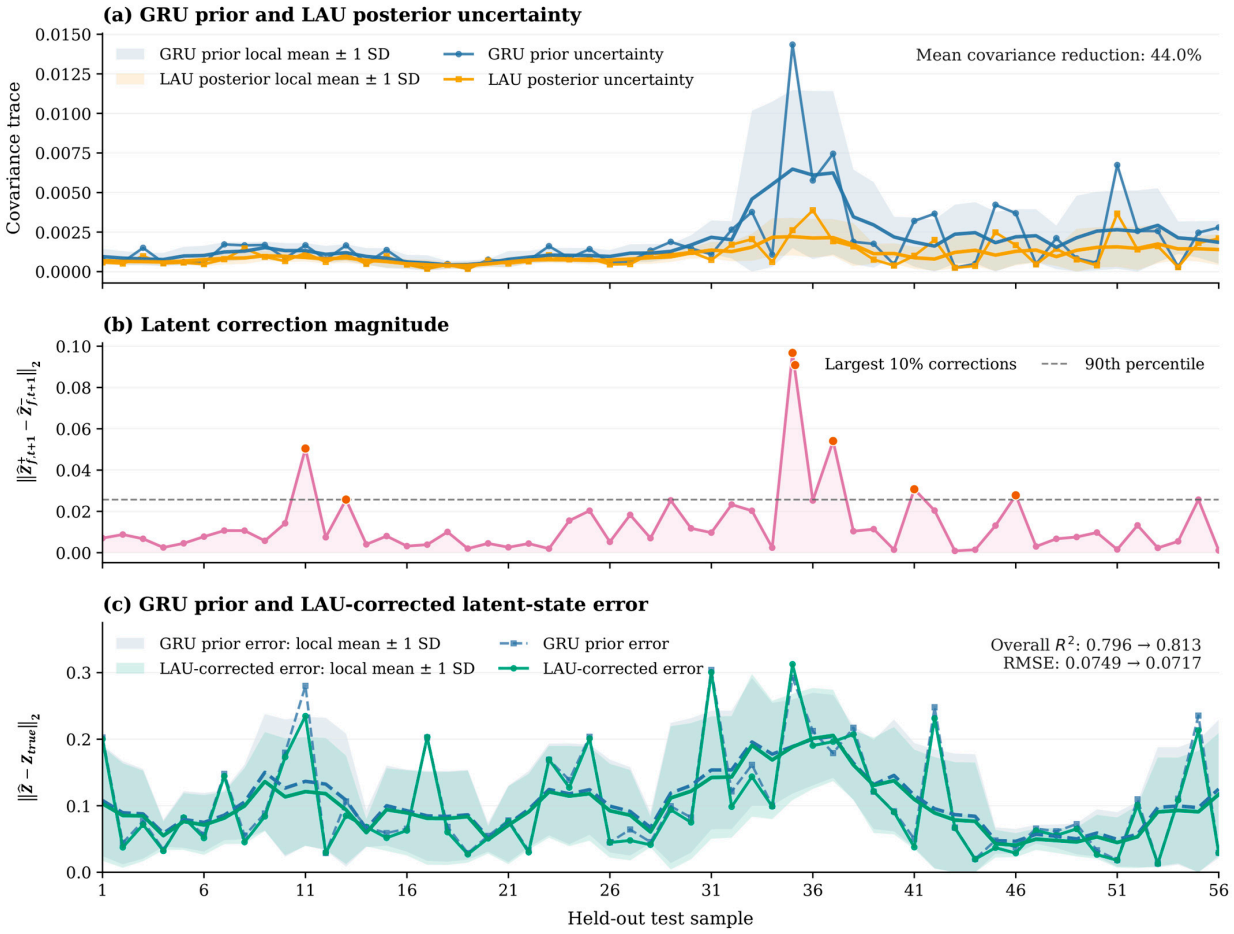


Figure 15. LAU-based latent-state synchronization on the held-out test set: (**a**) prior and posterior uncertainty, with shaded bands representing local mean ± 1 SD; (**b**) latent state correction magnitude, measured by the Euclidean norm $\|\cdot\|_2$; (**c**) latent-state error before and after assimilation. SD denotes standard deviation. In subfigure (**b**), the orange dots indicate the largest 10% of latent-state corrections by magnitude.

To compare the proposed synchronization methods, an ablation analysis was conducted. The evaluated methods include GRU-512 prior, Fixed-R LAU, RA-LAU, and J-RA-LAU. All parameters were selected using the validation set and fixed before evaluation on the held-out test set. The results are summarized in Table 13.

Table 13. Ablation analysis of the latent-state synchronization mechanisms on the held-out set.

Variable	R^2	MAE	RMSE
GRU-512 prior	0.7962	0.0517	0.0749
Fixed-R-LAU	0.8133	0.0483	0.0717
RA-LAU	0.8173	0.0476	0.0709
J-RA-LAU	0.8217	0.0473	0.0701

The ablation analysis showed improvement in latent-state estimation across these methods. The RMSE decreased across the evaluated methods from 0.0749 for GRU-512 prior, 0.0717 for fixed R-LAU, 0.0709 for RA-LAU, and 0.0701 for J-RA-LAU. J-RA-LAU showed the lowest RMSE among the evaluated methods.

Furthermore, five controlled climate-stress scenarios were evaluated with the GRU-512 model. Table 14 presents the mean changes in the latent components relative to the baseline.

Table 14. Baseline-relative latent-state responses under controlled climate-stress scenarios.

Scenario	ΔZ_1	ΔZ_2	ΔZ_3
Heat	−0.0616	0.1845	0.0736
Dry	0.0732	−0.0009	0.0105
Hot-Dry	0.0179	0.1836	0.0905
Atmospheric-Dryness	−0.0866	0.0326	0.1751
Compound-Stress	−0.0051	0.0342	0.1986

The proposed scenario sensitivity analysis demonstrates that the latent-state response depended on both climate forcing and the latent dimension. The Heat and Hot-Dry scenarios showed the strongest responses in Z_2, with values 0.1845 and 0.1836, respectively. Atmospheric-Dryness and Compound-Stress scenarios showed 0.1751 and 0.1986 in Z_3, respectively. The Dry scenario produced smaller changes in the Z_2 and Z_3 components.

The climate-stress scenarios were based on data from 2020–2024. Heat was represented by the monthly 90th percentile (P90) of temperature. Dry was represented by the 10th percentile (P10) of positive precipitation. Hot-Dry combined the Heat and Dry conditions. Atmospheric-Dryness was based on the high temperature, low humidity, and high solar radiation. Compound stress combined heat, precipitation deficit, low humidity, and high solar radiation.

The decoded biophysical responses under the controlled climate-stress scenarios are summarized in Table 15.

The climate-stress scenarios produced different latent-state and decoded responses in the NKAES LLP fields. For example, the Compound-Stress scenario showed the largest negative changes in the vegetation indices, with $\Delta NDVI = -0.0382$; $\Delta NDRE = -0.3825$. Atmospheric-Dryness also produced clear changes in NDVI and NDWI variables. The LST and SM responses varied among the scenarios.

Figure 16 illustrates the responses of the three latent dimensions under the controlled climate-stress scenarios. The latent responses differed among the scenarios and dimensions. The Heat and Hot-Dry scenarios produced the largest positive responses in Z_2. Atmospheric-Dryness and Compound-Stress produced the largest positive responses in Z_3. The Z_1 response was positive under Dry and Hot-Dry conditions and negative under Heat and Atmospheric-Dryness. These results demonstrate that the learned latent dimensions respond differently to controlled climate forcing.

Table 15. Decoded biophysical response under controlled climate-stress scenarios.

Scenario	ΔNDVI	Δ*NDRE*	Δ*NDWI*	Δ*LST*	Δ*SM*
Heat	0.0115	0.1197	−0.0076	−2.3677	−0.0337
Dry	−0.0045	−0.0464	−0.0012	1.3640	−0.0071
Hot-Dry	0.0061	0.0760	−0.0107	−0.9830	−0.0424
Atmospheric Dryness	−0.0302	−0.3110	−0.0415	−2.7253	−0.0192
Compound Stress	−0.0382	−0.3825	−0.0394	−1.2115	−0.0289

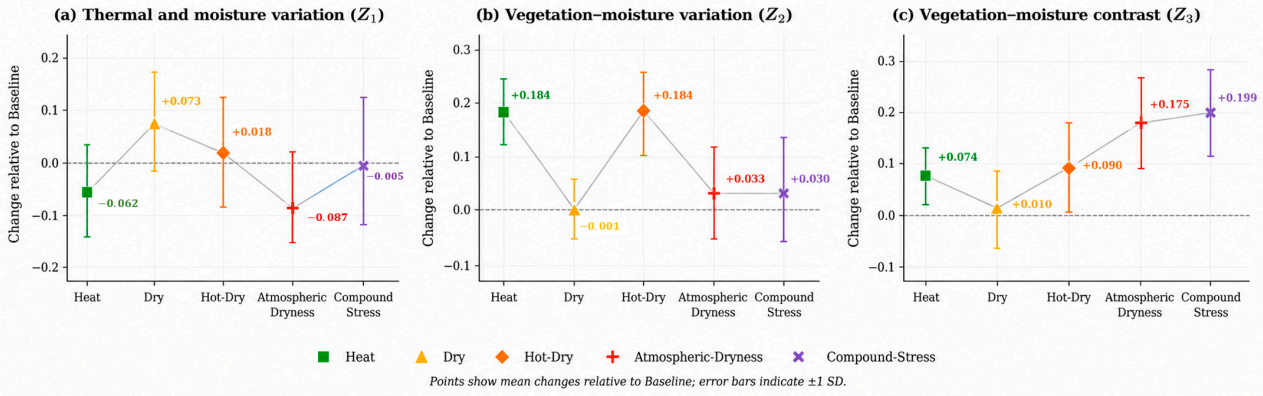


Figure 16. Latent-state responses to controlled climate-stress scenarios.

As shown in Figure 17, the spatial distribution of NDVI varied among the controlled climate-stress scenarios. Compared with the Baseline scenario, spatial changes in NDVI were observed under all climate-stress conditions.

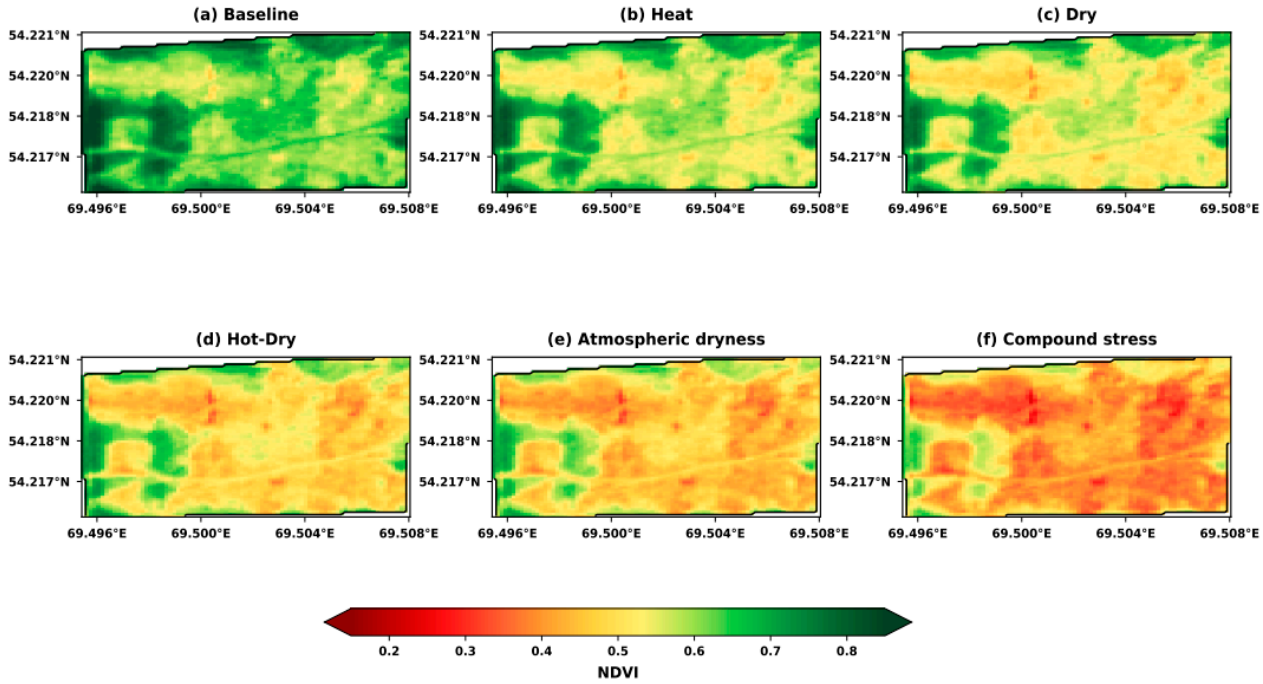


Figure 17. Spatial NDVI patterns under controlled climate-stress scenarios.

The changes were more pronounced under Atmospheric-Dryness and Compound-Stress. These results demonstrate the spatial variation in vegetation responses to climate stress.

4. Discussion

4.1. Interpretation of Results

This study proposed the integration of multi-sensor remote sensing data within a data-driven Digital Twin framework. The latent variables provide a concise representation of agroecosystem dynamics.

The information obtained from Sentinel-2, MODIS, and SMAP differs in spatial and temporal resolution. Therefore, data from the different sources were quality-filtered and temporally composited. This preprocessing made it possible to obtain a unified multidimensional time series for the agroecosystem on the agricultural lands under consideration.

First, a correlation analysis was performed on the data for the study area. As a result, high correlations were found among several optical indices. Therefore, only the NDVI, NDRE, NDWI, SM, and LST variables were retained. These variables provide complementary information on vegetation condition, chlorophyll-related characteristics, water availability, soil moisture, and thermal conditions.

This information is important for characterizing crop biophysical processes across different phenological stages.

Several models were evaluated in two- and three-dimensional spaces for encoding the Digital Twin variables into a latent space. The linear PCA method provided a strong baseline performance ($R^2 = 0.9800$).

However, it showed substantially higher seasonal drift (SD = 0.9766) than MLP-AE-3D. Therefore, several nonlinear autoencoders were considered. Among them, the three-dimensional MLP-AE model achieved good seasonal stability (SD = 0.2209) with a validation R^2 of 0.9554. These results indicate that MLP-AE-3D provided a better balance between reconstruction performance and seasonal stability.

A key component of the proposed framework is latent-state synchronization. The ablation analysis showed that Fixed-R LAU improved the GRU-512 prior. Reliability adaptation and decoder-sensitivity moderation provided further improvements. J-RA-LAU achieved the highest R^2 (0.8217) and the lowest RMSE (0.0701). This indicates that adaptive synchronization can further improve latent-state correction. However, the improvement over Fixed-R LAU was modest. The experiments used controlled synthetic latent observations. Therefore, the results support the potential of adaptive state synchronization rather than operational real-time simulation.

The climate scenario simulations in the proposed Digital Twin framework illustrate its scenario-analysis capability. By modifying climate-forcing variables, changes in latent states were observed. These latent-state changes were decoded to examine the corresponding responses of the reconstructed agroecosystem variables. Such experiments provide a controlled means of assessing the response of the learned agroecosystem representation to different climate-stress conditions.

4.2. Practical Implications for Sustainable Agroecosystem Management

The proposed Digital Twin framework provides a data-driven approach for supporting sustainable crop management. In this framework, datasets obtained from multiple sources are integrated into a unified latent space. The proposed architecture supports analysis of the agroecosystem state and modeling of its temporal evolution. It can help identify deviations from typical seasonal conditions and support field-level monitoring. The state-updating mechanism allows predicted latent states to be corrected when new observations become available. The framework relies on satellite-based observations without requiring IoT sensors.

4.3. Scalability and Generalizability

The study was conducted at NKAES LLP. The model was trained on data derived from globally available sources, including Sentinel-2, MODIS, SMAP, and NASA POWER. Nevertheless, the methodology can be adapted to other agricultural regions with similar climate conditions. The model should be retrained using local data when applied to a new region.

Furthermore, the proposed system is not limited to a single type of crop, such as spring wheat. The latent representations were trained from multisource data, rather than from empirical relationships specific to a single crop. This provides the potential for application to other crops. However, the system should be retrained and validated using crop-specific data.

4.4. Limitations

Despite its advantages, the framework also has some limitations. First, the framework was validated in one agricultural region. Before applying this methodology to another region, it is necessary to collect relevant remote sensing data for the local area. Revalidation using these data would therefore be required. During the analysis of climate scenarios, temperature, precipitation, humidity, and solar radiation were considered climate-forcing variables. These variables represent important climatic factors affecting agroecosystem conditions.

Furthermore, the proposed framework is based on remote sensing and meteorological data. Although the framework does not require additional infrastructure, it has not been validated with in situ sensor data or unmanned aerial vehicle (UAV) data.

In addition, monthly aggregation and the coarse spatial resolution of MODIS and SMAP may limit the representation of short-term and sub-field variability.

4.5. Future Research

Future research will extend the proposed framework using advanced temporal and spatial models, including transformer- and graph-based architectures. The validated components are being integrated into the AgroTwin platform. AgroTwin currently uses the VMAE-2D model and is regularly updated with real-world remote sensing data. Real-time validation of the newly developed components remains as future research. The platform supports field-level Earth observation visualization, agroecosystem state analysis, temporal prediction, and climate-scenario exploration. Representative interfaces are shown in Figure S1 of the Supplementary Materials.

5. Conclusions

This study developed a data-driven Digital Twin framework for agroecosystem state representation using multisource remote sensing data. The framework was evaluated for the NKAES LLP study area using Sentinel-2, MODIS, SMAP, and meteorological data.

The main results of the study are as follows:

- A modular Digital Twin framework was developed to integrate multisource Earth observation data within a common analytical structure. The framework combines latent-state synchronization, temporal prediction, and climate-scenario analysis.
- A nonlinear latent-state representation was implemented to capture vegetation, thermal, and soil moisture information in a common latent space. The MLP-AE-3D model provided high reconstruction performance with low seasonal drift and was retained as the latent-state encoder.
- The temporal evolution of the learned latent states was modeled using MLP, GRU, and TSN models with hidden dimensions of 128, 256, and 512. GRU-512 achieved the

best performance (Test $R^2 = 0.7962 \pm 0.0237$, Test RMSE $= 0.0749 \pm 0.0041$) and was selected as the temporal state-transition model.

- A Latent Assimilation Unit (LAU) based on Kalman filtering was implemented to synchronize predicted latent states with available observations. Assimilation improved the overall R^2 from 0.7962 to 0.8133 and reduced the RMSE from 0.0749 to 0.0717. The adaptive configurations further reduced the RMSE to 0.0709 for RA-LAU and 0.0701 for J-RA-LAU.
- Controlled climate-stress scenarios were used to evaluate the sensitivity of the learned latent states to changes in climatic conditions. The latent components showed distinct responses across Heat, Dry, Hot-Dry, Atmospheric-Dryness, and Compound-Stress scenarios. The decoded variables also showed spatially heterogeneous vegetation responses.

From a practical perspective, the Digital Twin framework integrates vegetation, thermal, and water conditions within a unified latent-state representation. It also supports climate-scenario analysis. These components provide a basis for field monitoring and assessing agroecosystem responses to environmental stress.

Integration of the latent Digital Twin framework into operational AgroTwin platform is underway. Future research will focus on real-time validation and exploring transformers, graph neural networks, and PINNS.

Supplementary Materials: The following supporting information can be downloaded at: https://www.mdpi.com/article/10.3390/su182110993/s1, Figure S1: Examples of the AgroTwin research prototype interfaces supporting agroecosystem monitoring and Digital Twin visualization; Table S1: Results of the temporal-smoothing sensitivity analysis.

Author Contributions: Conceptualization, A.M.; methodology, A.M.; software, A.M.; validation, A.M., S.K., and T.Z.; formal analysis, A.M.; investigation, A.M.; resources, T.Z.; data curation, A.M.; writing—original draft preparation, A.M.; writing—review and editing, S.K. and T.Z.; visualization, A.M. and V.M.; project administration, G.M. All authors have read and agreed to the published version of the manuscript.

Funding: This research received no external funding.

Institutional Review Board Statement: Not applicable.

Informed Consent Statement: Not applicable.

Data Availability Statement: The remote sensing data (Sentinel-2, MODIS, SMAP) used in this study are openly available through Google Earth Engine (GEE) and the NASA Earth Data Platform. The processed latent-state and climate datasets are available in the Zenodo repository: https://doi.org/10.5281/zenodo.23675113.

Acknowledgments: The authors thank the staff of NKAES LLP, particularly Oleg Solovyev, Head of the Crop Rotation and Soil Tillage Laboratory, for their valuable assistance. They also appreciate the information provided on the experimental fields, agricultural practices, and archival agronomic records. During manuscript preparation, the authors used ChatGPT (GPT-6, OpenAI) to create illustrative icons for schematic figures. The authors reviewed the output and take full responsibility for the publication content.

Conflicts of Interest: The authors declare no conflicts of interest.

Abbreviations

The following abbreviations are used in this manuscript:

Abbreviation	Definition
DT	Digital Twin
NDVI	Normalized Difference Vegetation Index
NDRE	Normalized Difference Red Edge
NDWI	Normalized Difference Water Index
LST	Land Surface Temperature
SM	Soil Moisture
PCA	Principal Component Analysis
MLP-AE	Multilayer Perceptron Autoencoder
GRU	Gated Recurrent Unit
TSN	Temporal Scenario Network
LAU	Latent Assimilation Unit
RMSE	Root Mean Square Error
MAE	Mean Absolute Error
PINN	Physics-Informed Neural Network

References

1. Kruize, J.W.; Wolfert, J.; Scholten, H.; Verdouw, C.N.; Kassahun, A.; Beulens, A.J.M. A reference architecture for Farm Software Ecosystems. *Comput. Electron. Agric.* **2016**, *125*, 12–28. [CrossRef]
2. Aldhahri, E.A.; Almazroi, A.A.; Alkinani, M.H.; Ayub, N.; Alghamdi, E.A.; Janbi, N.F. Smart Farming: Enhancing Urban Agriculture through Predictive Analytics and Resource Optimization. *IEEE Access* **2025**, *13*, 72375–72388. [CrossRef]
3. Barroso-Barroso, C.; Vega-Muñoz, A.; Maradiaga-López, J.; Salazar-Sepúlveda, G.; Carabantes-Silva, R. Smart Farming and the SDGs: Emerging Research Patterns and Sustainability Implications. *Agriculture* **2026**, *16*, 81. [CrossRef]
4. Eisfelder, C.; Boemke, B.; Gessner, U.; Sogno, P.; Alemu, G.; Hailu, R.; Mesmer, C.; Huth, J. Cropland and Crop Type Classification with Sentinel-1 and Sentinel-2 Time Series Using Google Earth Engine for Agricultural Monitoring in Ethiopia. *Remote Sens.* **2024**, *16*, 866. [CrossRef]
5. Felegari, S.; Sharifi, A.; Moravej, K.; Amin, M.; Golchin, A.; Muzirafuti, A.; Tariq, A.; Zhao, N. Integration of Sentinel 1 and Sentinel 2 Satellite Images for Crop Mapping. *Appl. Sci.* **2021**, *11*, 10104. [CrossRef]
6. Santana, C.T.C.d.; Adami, M.; Prudente, V.H.R.; Garcia, A.D.B.; Caldas, M.M. Using Harmonized Landsat Sentinel-2 Vegetation Indices to Estimate Sowing and Harvest Dates for Corn and Soybeans in Brazil. *Remote Sens.* **2025**, *17*, 2927. [CrossRef]
7. Mimenbayeva, A.; Zhukabayeva, T. A review of free resources for processing and analyzing geospatial data. In *Proceedings of the 6th International Conference on Engineering & MIS 2020*; ACM: New York, NY, USA, 2020; pp. 1–4. [CrossRef]
8. Wild, A.; Chua, Z.-W.; Kuleshov, Y. Evaluation of Satellite Precipitation Estimates over the South West Pacific Region. *Remote Sens.* **2021**, *13*, 3929. [CrossRef]
9. Radočaj, D.; Jurišić, M.; Plaščak, I.; Galić, L. Satellite Remote Sensing for Crop Yield Prediction: A Review. *Agriculture* **2026**, *16*, 417. [CrossRef]
10. Nițu, A.; Florea, C.; Ivanovici, M.; Racoviteanu, A. NDVI and Beyond: Vegetation Indices as Features for Crop Recognition and Segmentation in Hyperspectral Data. *Sensors* **2025**, *25*, 3817. [CrossRef] [PubMed]
11. Pal, A.K.; Patro, B.D.K.; Chaube, S. Design and implementation of a deep learning framework for automated crop classification and health diagnosis in precision agriculture. *Sci. Rep.* **2026**, *16*, 11436. [CrossRef] [PubMed]
12. Dong, F.; Qin, F.; Zhang, T.; Dong, X.; Wu, Y.; Guo, Z. kNDVI reveals vegetation dynamics and hydro–edaphic controls in inner Mongolia (2000–2024). *Sci. Rep.* **2026**, *16*, 5244. [CrossRef] [PubMed]
13. Abdali, E.; Valadan Zoej, M.J.; Taheri Dehkordi, A.; Ghaderpour, E. A Parallel-Cascaded Ensemble of Machine Learning Models for Crop Type Classification in Google Earth Engine Using Multi-Temporal Sentinel-1/2 and Landsat-8/9 Remote Sensing Data. *Remote Sens.* **2024**, *16*, 127. [CrossRef]
14. TaToktagulova, G.; Mimenbayeva, A.B. Analysis of Machine Learning Algorithms for Forecasting Harvest Data in Kazakhstan. In Proceedings of the 2024 IEEE 4th International Conference on Smart Information Systems and Technologies (SIST), Astana, Kazakhstan, 15–17 May 2024; pp. 530–535. [CrossRef]
15. Mimenbayeva, A.B.; Omirtay, M.; Niyazova, R.; Bekmagambetova, G.; Suleimenova, R.; Tursumbayeva, A. An Artificial Neural Network Model to Forecast Grain Crops in North-Kazakhstan Agricultural Experimental Station. In Proceedings of the 2023 4th International Conference on Communications, Information, Electronic and Energy Systems (CIEES), Plovdiv, Bulgaria, 23–25 November 2023; pp. 1–5. [CrossRef]

16. Ghaderpour, E.; Mazzanti, P.; Bozzano, F.; Scarascia Mugnozza, G. Trend Analysis of MODIS Land Surface Temperature and Land Cover in Central Italy. *Land* **2024**, *13*, 796. [CrossRef]
17. Dorigo, W.; Wagner, W.; Albergel, C.; Albrecht, F.; Balsamo, G.; Brocca, L.; Chung, D.; Ertl, M.; Forkel, M.; Gruber, A.; et al. ESA CCI Soil Moisture for improved Earth system understanding: State-of-the-art and future directions. *Remote Sens. Environ.* **2017**, *203*, 185–215. [CrossRef]
18. Babaeian, E.; Sadeghi, M.; Jones, S.B.; Montzka, C.; Vereecken, H.; Tuller, M. Ground, proximal, and satellite remote sensing of soil moisture. *Rev. Geophys.* **2019**, *57*, 530–616. [CrossRef]
19. Attema, E.P.W.; Ulaby, F.T. Vegetation modeled as a water cloud. *Radio Sci.* **1978**, *13*, 357–364. [CrossRef]
20. Gao, Q.; Zribi, M.; Escorihuela, M.J.; Baghdadi, N. Synergetic Use of Sentinel-1 and Sentinel-2 Data for Soil Moisture Mapping at 100 m Resolution. *Sensors* **2017**, *17*, 1966. [CrossRef] [PubMed]
21. Gargiulo, M.; Dell'Aglio, D.A.G.; Iodice, A.; Riccio, D.; Ruello, G. Integration of Sentinel-1 and Sentinel-2 Data for Land Cover Mapping Using W-Net. *Sensors* **2020**, *20*, 2969. [CrossRef] [PubMed]
22. Oroud, I.M.; Balling, R.C., Jr. The Utility of Combining Optical and Thermal Images in Monitoring Agricultural Drought in Semiarid Mediterranean Environments. *J. Arid Environ.* **2021**, *189*, 104499. [CrossRef]
23. Izquierdo-Sanz, H.; Moltó, E. Hybrid Physical–Machine Learning Soil Moisture Modeling at Orchard Scale in Irrigated Citrus Orchards Using Sentinel 1 and 2 and Agroclimatic Data. *Agronomy* **2026**, *16*, 541. [CrossRef]
24. Guo, Z.; Cheng, L.; Chang, L.; Li, S.; Li, Y. A Modified Method for Reducing the Scale Effect in Land Surface Temperature Downscaling at 10 m Resolution. *Remote Sens.* **2024**, *16*, 3908. [CrossRef]
25. Dorigo, W.; Gruber, A.; de Jeu, R.A.M.; Wagner, W.; Stacke, T.; Loew, A.; Albergel, C.; Brocca, L.; Chung, D.; Parinussa, R.M.; et al. Evaluation of the ESA CCI soil moisture product using ground-based observations. *Remote Sens. Environ.* **2015**, *162*, 380–395. [CrossRef]
26. Jolliffe, I.T.; Cadima, J. Principal component analysis: A review and recent developments. *Philos. Trans. R. Soc. A* **2016**, *374*, 20150202. [CrossRef]
27. Zhou, H.; Wang, F.; Tao, P. t-Distributed stochastic neighbor embedding (t-SNE) method with the least information loss for macromolecular simulations. *J. Chem. Theory Comput.* **2018**, *14*, 5499–5510. [CrossRef] [PubMed]
28. Lapenda, L.V.N.; Monteiro, R.P.; Bastos-Filho, C.J.A. Autoencoder latent space: An empirical study. In Proceedings of the 2020 IEEE Symposium Series on Computational Intelligence (SSCI), Canberra, Australia, 1–4 December 2020; pp. 2453–2460. [CrossRef]
29. Qiao, W.; Luo, D. An autoencoder-based framework for analyzing regional variations in urban green space demand. *Front. Sustain. Cities* **2025**, *7*, 1642184. [CrossRef]
30. Wang, Y.; Hernández Hernández, H.; Albrecht, C.M.; Zhu, X.X. Feature Guided Masked Autoencoder for Self-Supervised Learning in Remote Sensing. *IEEE J. Sel. Top. Appl. Earth Obs. Remote Sens.* **2025**, *18*, 321–336. [CrossRef]
31. Zhu, X.X.; Tuia, D.; Mou, L.; Xia, G.S.; Zhang, L.; Xu, F.; Fraundorfer, F. Deep learning in remote sensing: A comprehensive review and list of resources. *IEEE Geosci. Remote Sens. Mag.* **2017**, *5*, 8–36. [CrossRef]
32. Adrian, J.; Sagan, V.; Maimaitijiang, M. Sentinel SAR-optical fusion for crop type mapping using deep learning and Google Earth Engine. *ISPRS J. Photogramm. Remote Sens.* **2021**, *175*, 215–235. [CrossRef]
33. Berger, K.; Machwitz, M.; Kycko, M.; Kefauver, S.C.; van Wittenberghe, S.; Gerhards, M.; Verrelst, J.; Atzberger, C.; van der Tol, C.; Damm, A.; et al. Multi-Sensor Spectral Synergies for Crop Stress Detection and Monitoring in the Optical Domain: A Review. *Remote Sens. Environ.* **2022**, *280*, 113198. [CrossRef] [PubMed]
34. Meléndez, A.S.; Burry, L.S.; Palacio, P.I.; Trivi, M.E.; Quesada, M.N.; Freire, V.Z.; D'Antoni, H. Ecosystems dynamics and environmental management: An NDVI reconstruction model for El Alto-Ancasti mountain range (Catamarca, Argentina) from 442 AD through 1980 AD. *Quatern. Sci. Rev.* **2024**, *324*, 108450. [CrossRef]
35. Peters, J.; Mora, K.; Mahecha, M.D.; Ji, C.; Montero, D.; Mosig, C.; Kraemer, G. Context-Aware Multimodal Representation Learning for Spatio-Temporally Explicit Environmental Modeling. *IEEE Trans. Geosci. Remote Sens.* **2026**, *64*, 2669. [CrossRef]
36. Escribà-Gelonch, M.; Liang, S.; van Schalkwyk, P.; Fisk, I.; Long, N.V.D.; Hessel, V. Digital Twins in Agriculture: Orchestration and Applications. *J. Agric. Food Chem.* **2024**, *72*, 10737–10752. [CrossRef] [PubMed]
37. Kim, S.; Heo, S. An agricultural digital twin for mandarins demonstrates the potential for individualized agriculture. *Nat. Commun.* **2024**, *15*, 1561. [CrossRef] [PubMed]
38. Melesse, T.Y. Digital Twin-Based Applications in Crop Monitoring. *Heliyon* **2025**, *11*, e42137. [CrossRef] [PubMed]
39. Purcell, W.; Neubauer, T. Digital Twins in Agriculture: A State-of-the-Art Review. *Smart Agric. Technol.* **2023**, *3*, 100094. [CrossRef]
40. Tang, R.; Wu, L.; Wang, Z.; Zhu, L.; Sun, A.; Ru, Q.; Ju, B. Physics-Informed Neural Networks for Real-Time Updating and Synchronisation in Digital Twins: A Focused Review. *Digit. Twins Appl.* **2026**, *3*, e70042. [CrossRef]
41. Nearing, G.S.; Crow, W.T.; Thorp, K.R.; Moran, M.S.; Reichle, R.H.; Gupta, H.V. Assimilating Remote Sensing Observations of Leaf Area Index and Soil Moisture for Wheat Yield Estimates: An Observing System Simulation Experiment. *Water Resour. Res.* **2012**, *48*, W05525. [CrossRef]

42. Kritzinger, W.; Karner, M.; Traar, G.; Henjes, J.; Sihn, W. Digital Twin in manufacturing: A categorical literature review and classification. *IFAC-PapersOnLine* **2018**, *51*, 1016–1022. [CrossRef]
43. Pylianidis, C.; Osinga, S.; Athanasiadis, I.N. Introducing digital twins to agriculture. *Comput. Electron. Agric.* **2021**, *184*, 105942. [CrossRef]
44. Jones, D.; Snider, C.; Nassehi, A.; Yon, J.; Hicks, B. Characterising the Digital Twin: A systematic literature review. *CIRP J. Manuf. Sci. Technol.* **2020**, *29*, 36–52. [CrossRef]
45. Gund, R.; Badgujar, C.M.; Samiappan, S.; Jagadamma, S. Application of Digital Twin Technology in Smart Agriculture: A Bibliometric Review. *Agriculture* **2025**, *15*, 1799. [CrossRef]
46. Liu, X.; Jiang, D.; Tao, B.; Xiang, F.; Jiang, G.; Sun, Y.; Kong, J.; Li, G. A systematic review of digital twin about physical entities, virtual models, twin data, and applications. *Adv. Eng. Inform.* **2023**, *55*, 101876. [CrossRef]
47. Tagarakis, A.C.; Benos, L.; Kyriakarakos, G.; Pearson, S.; Sørensen, C.G.; Bochtis, D. Digital Twins in Agriculture and Forestry: A Review. *Sensors* **2024**, *24*, 3117. [CrossRef] [PubMed]
48. Wang, L. Digital Twins in Agriculture: A Review of Recent Progress and Open Issues. *Electronics* **2024**, *13*, 2209. [CrossRef]
49. Khan, T.; Bhatia, U.; Karmakar, S.; Kumar, V.; Mishra, V. Twin ECO: A unified framework for dynamic data-driven digital twins in ecology. *Ecol. Inform.* **2025**, *87*, 103407. [CrossRef]
50. Liu, W.; He, S.; Mou, J.; Xue, T.; Chen, H.; Xiong, W. Digital twins-based process monitoring for wastewater treatment processes. *Reliab. Eng. Syst. Saf.* **2023**, *240*, 109416. [CrossRef]
51. Joshi, A.; Pradhan, B.; Gite, S.; Chakraborty, S. Remote-Sensing Data and Deep-Learning Techniques in Crop Mapping and Yield Prediction: A Systematic Review. *Remote Sens.* **2023**, *15*, 2014. [CrossRef]
52. Chicco, D.; Warrens, M.J.; Jurman, G. The Coefficient of Determination R-Squared Is More Informative than SMAPE, MAE, MAPE, MSE and RMSE in Regression Analysis Evaluation. *PeerJ Comput. Sci.* **2021**, *7*, e623. [CrossRef] [PubMed]
53. Hodson, T.O. Root-Mean-Square Error (RMSE) or Mean Absolute Error (MAE): When to Use Them or Not. *Geosci. Model Dev.* **2022**, *15*, 5481–5487. [CrossRef]
54. Boiarskii, B.; Hasegawa, H. Comparison of NDVI and NDRE Indices to Detect Differences in Vegetation and Chlorophyll Content. *J. Mech. Contin. Math. Sci.* **2019**, *4*, 20–29. [CrossRef]

Disclaimer/Publisher's Note: The statements, opinions and data contained in all publications are solely those of the individual author(s) and contributor(s) and not of MDPI and/or the editor(s). MDPI and/or the editor(s) disclaim responsibility for any injury to people or property resulting from any ideas, methods, instructions or products referred to in the content.